Laboratory acousto-mechanical study into moisture-induced changes of elastic properties in intact granite

Rui Wu[1], Paul Antony Selvadurai[1], Ying Li[1], Yongyang Sun[2], Kerry Leith[1], Simon Loew[1]

[1]Department of Earth Science, ETH Zürich, Zürich, Switzerland.
[2]Department of Exploration Geophysics, Curtin University, Perth, Australia.

Key Points:

- Laboratory time-lapse acousto-mechanical response of a freestanding intact granite specimen experiencing gradually wetting over 98 hours.
- Squirt flow dominates P-wave velocity dispersion from extensional to contractional stress regimes in microcracked nanopore-dominated media.
- Changes in transmitted energy and corner frequency are explained and predicted by elastic wave propagation around P-wave first Fresnel zone.

Corresponding author: Rui Wu, `rui.wu@erdw.ethz.ch`

Abstract

The water adsorption into pore spaces in brittle rocks affects wave velocity, transmitted energy and corner frequency of transmitted elastic waves. Experimental and theoretical studies have been performed to characterize moisture-induced elastodynamic variations due to macroporous effects; however, little attention has been paid to the manner in which wetting of nanopores affect elastic wave transmission. In this work, we extend our understanding of moisture-induced elastic changes in a microcracked nanopore-dominated medium (80 % of the surface area exhibits pore diameters below 10 nm). We studied acousto-mechanical response resulting from a gradual wetting on a freestanding intact Herrnholz granite specimen over 98 hours using time-lapse ultrasonic and digital imaging techniques. Linkages between acoustic attributes and adsorption-induced stress/strain are established during the approach of wetting front. We found that Gassmann theory, previously validated in channel-like nanoporous media, breaks down in predicting P-wave velocity dispersion of microcracked nanopore-dominated media. However, squirt flow – a theory recognized to characterize wave dispersion and attenuation in microcracked macropore-dominated media at pore scale – also accounts for the observed dispersion of P-wave velocity in microcracked nanopore-dominated media spanning stress regimes in both contraction and extension. The transmitted energy change and the corner frequency shift in direct P waves are explained and predicted by the elastic wave propagation within P-wave first Fresnel zone and reflection on the wetting front.

Plain Language Summary

Rainfall, melting snow, dew, and fog that occurs at the earth's surface have all been shown to perturb elastic wave travel times, and decrease the amplitude of transmitted elastic waves in crustal rocks. This moisture-induced elastic variation is highlighted in the stability of engineering structures (e.g. bridges, dams), geo-energy extraction, and landslide behavior. The observed elastic variations have been studied, particularly in rocks with cracks, by analyzing the propagation perturbation of the transmitted elastic waves. However, very little is known about how elastic waves change with water imbibition in intact rocks. In this study, a noninvasive assessment technique named as ultrasonic monitoring is utilized to probe natural nanopore-dominated granite undergoing gradual wetting. We observed that a shorter P-wave travel time can be attributed to the pore fluid squirt from microcracks into relatively round pore spaces. Changes in the transmitted energy and corner frequency around the P-wave onset is mainly caused by incident P-wave reflection and conversion on the moving water front. Acoustic results are corroborated by simultaneous monitoring of the mechanical deformation.

1 Introduction

In the earth's crust, fluids can alter the material properties from near-surface to subsurface in various ways. Natural (e.g. precipitation, dew, fog, melting snow) or anthropogenic hydraulic activities (e.g. water injection, hydrocarbon production) can increase the moisture content of porous medium driven by capillary pressure, gravity and injection pressure differences. During wetting, water molecules are initially adsorbed onto grain boundaries followed by capillary condensation; liquids gradually fill, and (almost) fully saturate the interconnected pore space (Gor & Neimark, 2010; Gor & Bernstein, 2016). This process induces changes in elastic properties; these have been reported in numerous *in situ* observations, varying from near-surface natural hazards, e.g. landslides related to groundwater movement or rainfall (Loew et al., 2017; Burjánek et al., 2017; Le Breton et al., 2021), engineering structure stability, e.g. thin sheet collapse of borehole/tunnelling wall (Diederichs, 2007), building material decay due to fluctuating humidity (McBain & Ferguson, 2002); and subsurface geo-energy applications involving with water flooding, e.g. oil and gas recovery, geothermal energy extraction (Landrø, 2001). Observed moisture-induced elastic variation almost always change the propagation of elastic waves in host materials. Characterization of moisture-induced variation of elastic properties, using the theory of elastic wave propagation, plays a central role in rock-physics research (Saito, 1981; Barton, 2006; Mavko et al., 2020).

1.1 Background on elastic response of porous media during water imbibition

The study of the dynamic elastic response of porous media to water imbibition has been reported from numerous laboratory and analytical studies performed on dry and saturated (un)stressed rocks over the past 70 years (Gassmann, 1951; Nur & Simmons, 1969; Winkler & Nur, 1979; Toksöz et al., 1979; Johnston et al., 1979; Mavko & Nur, 1979; Murphy III, 1982; Knight & Nolen-Hoeksema, 1990; Walsh, 1995; Barton, 2006; Gurevich et al., 2010; Mavko et al., 2020). High-frequency elastic waves (usually tens of kHz to MHz for laboratory measurements) are produced by ultrasonic piezoelectric actuators and are then detected by ultrasonic receivers, which use the amplitude and wave velocity information to estimate their sensitivity to the presence of pore fluid. There is a large compendium of research on the underlying mechanisms of elastic changes due to moisture ingress into macroscopic pores; however, little attention has been paid to nanopores with pore widths below 100 nm defined by Thommes et al. (2015). This gap in the experimental understanding to explain the differences between wave propagation in macropore- and nanopore-dominated media lead to this study.

In laboratory tests, the P-wave velocity is widely observed to increase when macroporous, clay-deficient rocks become (almost) fully saturated with water. This behavior is called "P-wave velocity dispersion" and P-wave velocity increase has been reported in sandstone as 8 to 73 % (King, 1966; Han, 1987; Coyner, 1984; Mavko & Jizba, 1991; Wang et al., 2021); granite as 8 to 27 % (Nur & Simmons, 1969; Saito, 1981; Coyner, 1984); limestone as 0 to 73 % (Nur & Simmons, 1969; Coyner, 1984; Agersborg et al., 2008) and dolomite as 28 % (Nur & Simmons, 1969). Various physical mechanisms have been proposed to predict such P-wave velocity dispersion; for example, Gassmann's equation (Gassmann, 1951), Biot's theory (Biot, 1956) and the squirt flow model (Mavko & Jizba, 1991; Gurevich et al., 2010). Extensive review of these models are given by Müller et al. (2010) and Mavko et al. (2020, Chapter 6).

Gor and Gurevich (2018) accurately modeled P-wave modulus changes in Vycor glass saturated by n-hexane (Page et al., 1995) and argon (Schappert & Pelster, 2013) within the framework of classical Gassmann theory (Gassmann, 1951; Berryman, 1999). Vycor glass in their study is a well-defined nanoporous medium characterized by channel-like pores with a peak throat size of around 7 to 8 nm (Levitz et al., 1991). However, natural nanoporous media such as rocks, some are characterized by grain boundary cracks, intragranular cracks, and intergranular cracks. Microcrack-based microstructures contribute to the bulk elastic changes more than round pores under varying confining pressure (Shapiro, 2003) or with the addition of pore fluid (O'Connell & Budiansky, 1977). It is premature to extend the validity of Gassmann theory to nanopores in microcracked media due to the added complexities of microcracks not present in the man-made Vycor glass (Gor & Gurevich, 2018; Dobrzanski et al., 2021). To the authors' knowledge, there are no classical theories (e.g. Gassmann theory) relevant to materials that contain both nanopores and microcracks. As almost all natural rocks contain a full range of pore sizes, understanding such material is fundamental to earth science researches.

Acoustic transmitted energy has been linked to the elastic properties of porous media (Barton, 2006; Mavko et al., 2020) and it is more sensitive than wave velocity to increases in the moisture content. Studies show that observed losses in transmitted energy are an order of magnitude larger than variations in wave velocity (Winkler & Nur, 1979, 1982; David, Sarout, et al., 2017). During water imbibition tests on rocks (Wulff & Mjaaland, 2002; David, Sarout, et al., 2017; Pimienta et al., 2019; Thery et al., 2020), the mechanism driving the wetting front is capillary force, where free water first wets or saturates compliant microcracks at the grain scale. In nanoporous material, during water imbibition, fluid (or solvation) pressure inside the nanopores is generated (Gor & Neimark, 2010; Gor & Bernstein, 2016), which decreases the normal stress across microcracks (Li et al., 2021). This process also decreases contact stiffness across microcracks (Yurikov et al., 2018) and friction coefficient along microcracks (Johnston et al., 1979). Passage of the fully elastic waves causes more relative normal and shear deformation across and along microcracks at the grain scale; as a result, more transmitted energy can be dissipated (Barton, 2006).

When analyzing the transmitted energy in the frequency domain (Stoica et al., 2005), the characteristic frequency of the energy spectra also reflects the elasticity of the unforced multiple degree-of-freedom system. A higher characteristic frequency suggests larger elastic moduli of the measured objects (Christaras et al., 1994; Shabana, 2018). This has been recently applied to the *in situ* monitoring and characterization of rock mass (in)stability (Moore et al., 2018, 2019; Burjánek et al., 2019; Häusler et al., 2019, 2021). Between November 2012 and September 2013 Burjánek et al. (2017) monitored the ambient vibration of an unstable rock slope that had a long history of catastrophic failures (Loew et al., 2017). Burjánek et al. (2017) noticed that precipitation events (daily precipitation up to 25 mm) in April/May 2013 increased the moisture content of rock mass and might be related to the simultaneous decrease in resonant frequencies (3.7 down to 3.3 Hz). However, the root cause is not yet fully clear because resonant frequencies exhibit more regular changes due to other environmental factors such as seasonal temperature variations.

Acoustic-derived changes in elastic properties can be better understood if simultaneous low-frequency mechanical deformation data is available. Ultrasonic monitoring and mechanical deformation measurements have been jointly performed in macropore-dominated rocks, e.g. Bentheim sandstone (Yurikov et al., 2018) and Thüringer sandstone (Tiennot & Fortin, 2020). Most of pore diameters were measured as 40 μm (Saenger et al., 2016) for Bentheim sandstone. Yurikov et al. (2018) quantified adsorption-induced deformation (extensional strain of the order of 10^{-4}) and elastic modulus reduction (e.g. a P-wave velocity decrease of 13 to 16 %) when the relative humidity (RH) was gradually increased from 13 to 97 %. They attributed that the observed elastic weakening/softening to be the result of solvation pressure generated in the pore space (2 to 3 MPa in Bentheim sandstone and 18 MPa in Thüringer sandstone). Li et al. (2021) moved the focus from macropore- to nanopore-dominated rocks by studying Herrnholz granite, where the majority of pore diameters are below 10 nm. They gradually wet two free-standing 90 × 65 × 35 mm Herrnholz granite prisms using distilled water, which maintained water ingress from their upper surfaces. Using digital image correlation (DIC) techniques, they found extensional strain with magnitudes up to 4.7×10^{-4} on the front face of prisms and calculated a solvation pressure of 40 to 47 MPa. This provided the initial mechanical constraints of the "hygroscopic expansion" process in this geomaterial.

1.2 Our study

There are no studies on the acousto-mechanical response to water imbibition in media containing nanopores and microcracks with the approach of a wetting front. It is not yet clear how P-wave velocity, transmitted energy and characteristic frequency respond as the water is imbibed into the nanopore space. Moreover, these changes in the acoustic features have not been compared with adsorption-induced deformation at relatively low frequencies. To this end, we conducted time-lapse ultrasonic pulse transmission in conjunction with DIC measurements in the Herrnholz granite subject to wetting. Acoustic signature changes were analyzed: P-wave velocity, transmitted energy and corner frequency. We modeled the P-wave velocity changes with complementary hydrostatic compression tests. We also analyzed changes in acoustic energy from two separate wave phases (direct P and coda waves) and corner frequency during the approach of a wetting front while simultaneously monitoring the adsorption-induced deformation throughout the entire experiment.

2 Material description

The Herrnholz granite used in these tests was obtained from the eastern side of a rock quarry located in Hauzenberg, Bavaria Germany. The rock contains nanopores and microcracks and exhibits a homogeneous fine-grained structure; it has been well characterized with respect to its petrophysical and geomechanical properties in recent studies (Li et al., 2021, 2022).

2.1 Thin section analysis

Petrographic thin section analysis of selected specimens (35 mm $\times$ 22 mm $\times$ $30 \pm 5 \mu m$) revealed a granitic mineralogical assemblage of 50 % quartz, 38 % feldspar, and 11 % mica by area (Li et al., 2021). Crystal sizes range from approximately 0.03 to 1 mm with an average size of 0.23 mm and a standard deviation of 0.13 mm. In Figure 1, thin sections dyed with a fluorescent pigment showed the distribution and types of microcracks. Four classes of microcracks were revealed to exist: cleavage cracks, grain boundary cracks, intergranular cracks and intragranular cracks.

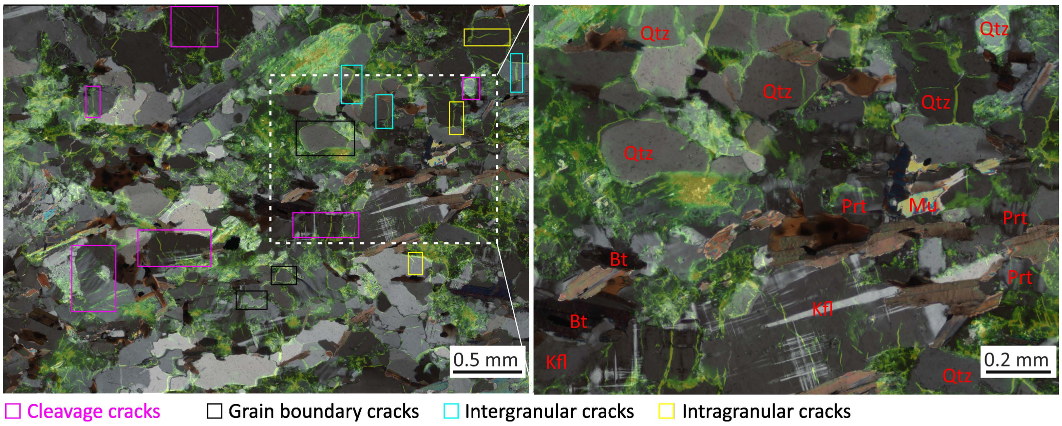

Figure 1. Superimposed micromosaic obtained with crossed-polarized light and ultraviolet light, indicating regions of cleavage cracks (purple box), grain boundary cracks (black box), intergranular cracks (cyan box) and intragranular (yellow box) cracks (Qtz: quartz; Kfl: K-feldspar; Prt: perthite; Bt: biotite; Mu:muscovite) (adapted from Li et al. (2021))

2.2 Porosity and pore size distribution

The porosity and pore size distribution were quantified using a combination of mercury intrusion, nitrogen adsorption, and water saturation methods. The grain density was estimated as 2.70 g/cm^3. Bulk density was measured under ambient conditions as the ratio of weight to volume, 2.64 g/cm^3. The density difference provided us a total porosity of 2.31 %. Mercury porosimetry was determined for seven specimens (20 mm $\times$ 6.5 mm $\times$ 6.5 mm). Mercury-accessible porosity ranged from to 0.72 % to 1.69 % with an mean porosity of around 1.15 %. Water-accessible porosity was estimated to be between 1.45 % and 1.53 % over three granite cylinders (100 mm in length, 50 mm in diameter) saturated by a de-airing technique (Selvadurai et al., 2011) lasting for 10 days. Detailed measurement method of water-accessible porosity are provided in Section 1 of the Supporting Information.

Poorly connected pores and pores with a throat diameter less than 10 nm are not open to mercury even at intrusive pressures up to 400 MPa. These pore volumes are not counted into the mercury-accessible porosity (1.15 %), and are assumed to contribute to the difference between the total and mercury-accessible porosity. To quantify the pore size distribution below 10 nm, Li et al. (2022) conducted nitrogen adsorption porosimetry over two specimens (40 mm × 10.5 mm × 10.5 mm) and revealed that around 80 % of the surface area of this granite exhibits pore diameter below 10 nm.

2.3 Ambient P-wave velocity measurement

A suite of characterization tests were performed to quantify the P wave velocity structure of our Herrnholz granite. We performed 3D ultrasonic tomography (Martiartu & Böhm, 2017) on three cuboidal specimens of granite with a side length of 160 mm under ambient conditions. Detailed experimental setup, measurement methodology, and visualization of the P-wave velocity structure are provided in Section 2 of the Supporting Information. P-wave velocity structure and the P-wave velocity in each orthogonal direction were experimentally characterized and uniform, with 3981 ± 69, 3977 ± 60, 3988 ± 64 m/s, respectively. The coefficients of variation were calculated as 1.72 %, 1.53 % and 1.60 %, respectively. To avoid specimen variability, we repeated the tests on other 2 specimens and found P-wave velocity of 3914 ± 74, 3925 ± 71, 3982 ± 64 m/s, respectively, with coefficients of variation of 1.9 %, 1.8 % and 1.6 %, respectively. We concluded that there is very weak anisotropy, heterogeneity and specimen variability in the elastic moduli of Herrnholz granite.

2.4 Elastic piezosensitivity

We analyzed the stress dependence of the dynamic elasticity of Herrnholz granite from separate hydrostatic compression tests. Basically an over-dried and saturated granite, and an aluminum (for reference) specimens were tested under stepwise-increasing axial and confining pressure from 5 to 160 MPa. The detailed experimental facilities and design (e.g. loading rate) are described in Section 3 of the supporting information. The measured P- and S-wave velocities of an oven-dried granite specimen (red circles) increase nonlinearly with the confining pressure P_c (5 to 160 MPa) from 4450 to 5731 m/s ($\Delta V_p = 1281$ m/s) and 2736 to 3311 m/s (ΔV_s = 575 m/s), as shown in Figure 2(a) and (b), respectively. Overlapped symbols denote repeated pulsing tests (about 50) at each confining pressure. The P-wave velocity in the saturated granite specimen (blue squares) increased from 5271 to 5804 m/s ($\Delta V_p = 533$ m/s) while corresponding S-wave velocity was not captured. Almost constant P- ($\Delta V_p = 60$ m/s) and slowly increasing S-wave ($\Delta V_s = 103$ m/s) velocities were found in the reference test Aluminum specimen (grey crosses). We derived the secant slopes of $\Delta V_p/P_c$ and $\Delta V_s/P_c$ as around 8.3 and 3.7 m/s/MPa in the granite specimen comparing to 0.39 and 0.66 m/s/MPa in the Aluminum specimen. No clear stress dependency of the elastic wave velocity was observed in the Aluminum specimen.

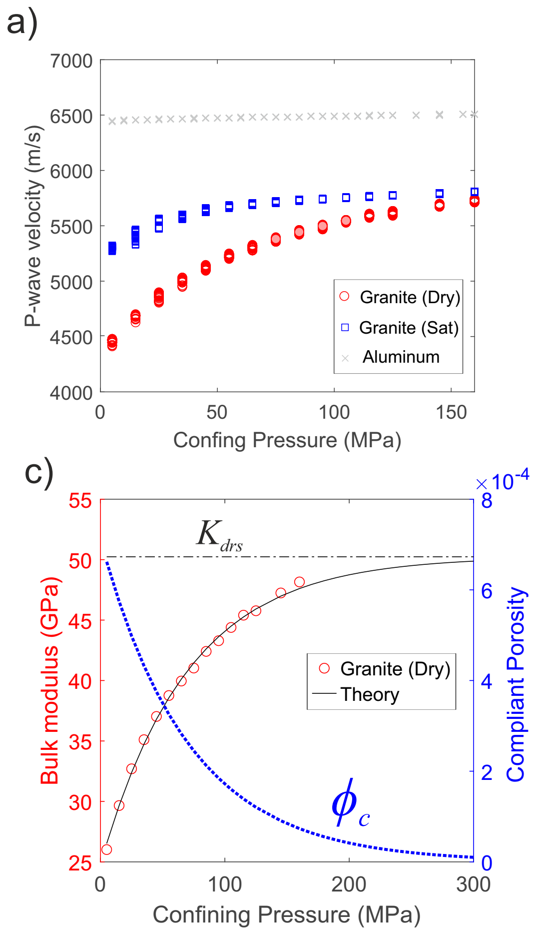

Figure 2. Stress dependence analysis of elasticity. (a) P- and (b) S-wave velocity changes in Herrnholz granite (red circles) and Aluminmum specimen (grey crosses) in response to a series of confining pressures (5 to 160 MPa). (c) Bulk and (d) shear moduli versus confining pressure (red circles: testing data; black lines: fitted results). Blue dashed line represents the compliant porosity evolution.

Given the bulk density of dry Herrnholz granite (2.64 g/cm^3) and confining pressure (P_c: 5 to 160 MPa), the dynamic bulk (K_{dry}) and shear (G_{dry}) moduli show a linear increase (grey dashed line) at low confining pressure (e.g. below 50 MPa) followed by a nonlinear rise at high confining pressure (Figure 2(c) and (d)). K_{dry} and G_{dry} range from 26.0 to 48.2 GPa and 19.8 to 28.9 GPa, respectively. In order to evaluate the effect of microcracks on this stress-dependent elasticity increase, we adopt a model of elastic piezosensitvity by Shapiro (2003). The theory assumes penny-shaped microcracks within a framework of effective medium theories. Porosity $\phi_c = 7.1 \times 10^{-4}$ and representative aspect ratio $\alpha = 1.1 \times 10^{-3}$ were derived for penny-shaped microcracks. The bulk (K_{drs}) and shear (G_{drs}) moduli of the granite without pore space were calculated as 50.4 and 30 GPa, respectively. Detailed mathematical description and parameter calculation of the elastic piezosensitive model are given in Section 3 of the Supporting Information.

In Figure 2(c) and (d), K_{dry} and G_{dry} (black solid line) derived from theory matched well the measured data (red circles). Above 160 MPa, the theoretical solutions gradually approach constant values (black dashed line) which are given by K_{drs} and G_{drs}. Compliant porosity ϕ_c (blue dashed line) decreases by two orders of magnitude: 7.1×10^{-4} at 0 MPa to 1×10^{-5} at 300 MPa, which is almost completely closed. 7.1×10^{-4} at 0 MPa is the compliant porosity without confinement (denoted as ϕ_{c0}). These piezosensitive parameters will be used in the P-wave velocity dispersion modeling later.

3 Free-standing wetting test

The aim of the main experiment reported in this study is to understand the acousto-mechanical response in nanopore-dominated geomaterials that experience hygroscopic expansion in response to gradual wetting. To quantify this effect, we build on the time-lapse monitoring methods of ultrasonic (Yurikov et al., 2018) and digital image correlation (DIC) (Li et al., 2021) methods in the Herrnholz granite.

3.1 General setup

Water imbibition tests were performed on an intact, free-standing "prismoid" specimen of Herrnholz granite (dimension: 65 × 35 × 90 mm) as shown in Figure 3(a). The specimen was initially oven-dried and then allowed to naturally acclimate to ambient conditions for 18 hours. Water was introduced to the specimen via a filter paper that was immersed in a water reservoir (∼15 mm above the specimen). Aluminium blocks kept the filter paper in contact with the top of the specimen and water was drawn onto the top surface by capillary forces. Distilled water was used to fill and replenish the reservoir (0, 26, 47, 71 hours) over 80 hours. This ensured an almost constant infiltration and imbibition of fluids into the top half of the sample that contained the region of interest (ROI) for the DIC measurements.

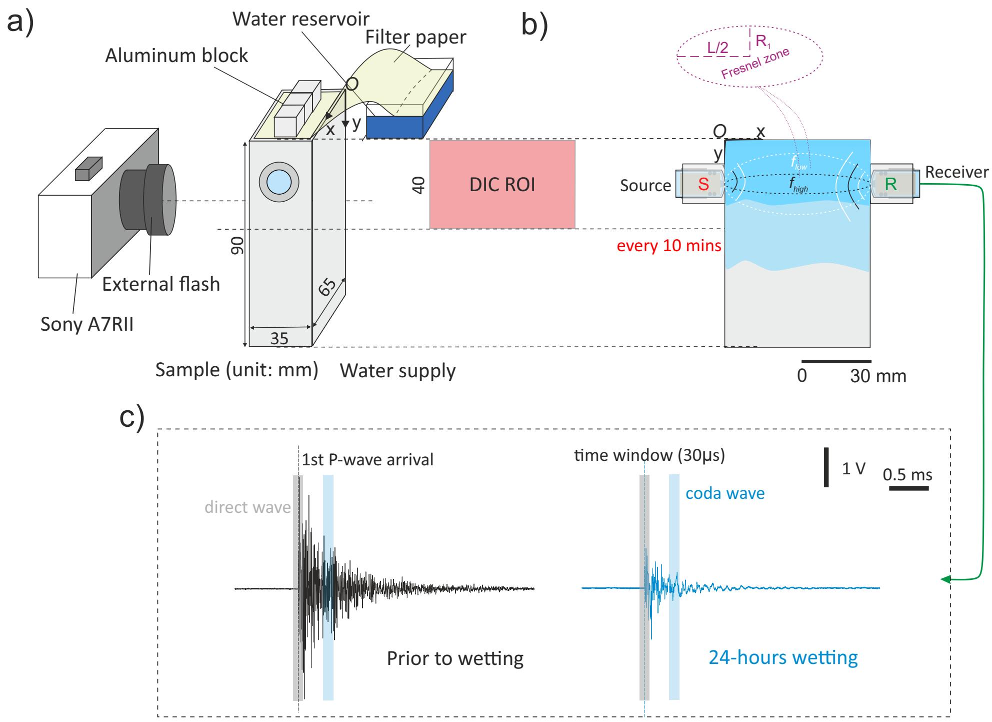

Figure 3. Schematic diagram of the experimental setup. (a) A free-standing granite prism (90 × 65 × 35 mm) of which upper part was subjected to gradual wetting. Mechanical moisture-induced deformation was measured on the vertical front surface in the region of interest (ROI) using digital image correlation (DIC). (b) Ultrasonic pulsing was performed using a PZT actuator coupled to the vertical surface 20 mm from the top of the sample. (c) Transmitted waveforms were monitored on a PZT receiver; dry (black) and wet (blue) measurements.

3.2 Time-lapse DIC observation

A time-lapse DIC technique was utilized to measure the moisture-induced deformation on the front face of the granite specimen. The fine crystalline nature of Herrnholz granite provides a suitable natural texture for DIC analysis. In Figure 3(a) a schematic depiction of the digital camera (Sony Alpha A7RII) is shown; this was mounted and locked to position

240 mm from the surface of the specimen. The front surface of the specimen was imaged at 2-minute intervals and 1/13-second exposure time. A low-power Sony LED macro flash was triggered by the camera shutter in order to create consistent lighting for the images without affecting the specimen temperature.

Prior to introducing water, the specimen was allowed to equilibrate for 18 hours at ambient conditions. This allowed us to evaluate the displacement and strain baselines in the absence of water. The region of interest (ROI), as shown as the pink patch in Figure 3(b), was located 3 - 4 mm from the top and side edges to minimize boundary effect, with 58 mm in width and 40 mm in height (symmetrical about the source-receiver y position). The displacement radius was 50 px or 0.8 mm (equivalent to several crystals given the mean grain size of 0.23 mm). The original ROI was 3–4 mm from the top and side edges to minimize boundary effects in the DIC. We used the open source Ncorr software (Blaber & Antoniou, 2015) to calculate the surface deformation at a resolution of 0.8 mm (equivalent to several grain sizes). For details related to parameter settings on the camera and DIC analysis (e.g. strain/displacement calculation, subset radius, resolution), we refer the reader to Li et al. (2021).

3.3 Time-lapse ultrasonic monitoring

To study changes in the acoustic signature in response to water imbibition, we adopted a time-lapse ultrasonic pulse transmission technique (Birch, 1960; ASTM D-18, 2008; Aydin, 2015). Figure 3(b) shows the PCT-MCX actuator (left, red S) and the KRNBB-PC receiver (right, green R) that were installed using aluminum cylinder holders at the height of $y = 20$ mm. The aluminum holders were coupled directly to the sample surface using cyanoacrylate and were threaded; this allowed the ultrasonic transducers to press against the surface of the specimen with their threaded casing. For this test, a high-voltage impulse source of 500 V was applied to the PCT-MCX actuator using the same pulsing system described in Section 2 of Supporting Information. Pulses were emitted every 10 minutes over $\sim$ 98 hours. Recordings were taken around the trigger (before: 0.5 ms, after: 2 ms) to fully capture all the wave information used in our analysis. Due to the more rapid transient response of the rock during the initial portions of the wetting, pulsing was performed every 2 minutes for 2 hours after wetting commenced. Waveforms of the receiver were recorded at 20 MHz. the same DAQ system and P-wave arrival picker were used as in Section 2.3.

3.4 Frequency-based volume of the Fresnel zone

The source-receiver arrangement generates a Fresnel zone, defined as a confocal prolate ellipsoidal region between source and receiver (Spetzler & Snieder, 2004). A schematic representation is shown in Figure 3(b) but the size of the Fresnel zone is dependent on the sample half width ($L = 65$ mm) and the frequency bandwidth of interest. Since the Fresnel zone has an ellipsoidal geometry, we use the same nomenclature as an ellipse to describe the Fresnel zone. The elastic properties of this zone are mostly revealed by direct waves propagating along the source-receiver straight ray path. The boundary of the Fresnel zone consists of points at which the difference in the propagation distance between direct and reflected waves is a multiple (n) of the half wavelength λ. In this study, we focus on the P-wave first ($n = 1$) Fresnel zone (P-FFZ), which gives the radius R_1 of the ellipsoid minor axis as:

$$R_1 = \frac{1}{2}\sqrt{\lambda L + \frac{\lambda^2}{4}}. \quad (1)$$

Equation (1) is only valid for a homogeneous medium. In our experiment it provides a rough estimate of R_1 when the wetting front moves towards the bottom surface, with introduced heterogeneity around the source-receiver straight ray path.

3.5 Data reduction techniques

Examples of waveforms derived from a dry and wet test stage (black: dry and blue: wet) show significantly attenuated elastic waves due to water ingress in Figure 3(c). Waveforms within the grey box represent the direct waves that mostly exhibit elastic changes in P-FFZ. To quantify the attenuation effect, the fast Fourier transform (Bracewell, 1986) was performed to study the spectral content of transmitted energy or energy spectral density from 100 kHz to 1 MHz. To avoid spectral leakage and focus the analysis on the direct P-wave phase, the waveform is windowed using a Blackmann-Harris window centered about the onset of first P-wave arrival. The P-wave arrival is calculated using the same AIC technique for P-wave velocity estimation. The window duration (e.g. grey box width) of 30 μs (roughly twice the travel time from source to receiver) is set to ensure that it will contain essential information on the direct P-wave phases and also at a satisfactory resolution $\sim$ 100 kHz, which is defined by Wu et al. (2021).

Coda waves (blue box in Figure 3(c)) are studied using the same spectral analysis technique as for direct waves. The onset of coda waves is set as 200 μs away from the triggering time of the source. This time difference is approximately 14 to 16 times of the P-wave travel time from source to receiver and ensures that the receiver acquires sufficient wave phases scattered by increasing the moisture-induced heterogeneity, as well as the outer boundaries. We noticed that waveforms acquired at sufficient wetting could merge into the noise level at 0 dB amplification. Thus a 40 dB gain was adopted to ensure extraction of the necessary message throughout the entire wetting stage.

4 Results

4.1 Moisture-induced changes in acoustic signatures

We analyzed the acoustic signature changes in transmitted direct and coda wave phases over 98 hours (18 hours under ambient conditions and 80 hours of wetting). Figure 4(a) shows the stacked and aligned raw waveforms of 630 events and a visualization of the direct wave phases from 5 to 25 μs. An acoustic duration equal to 0 μs refers to the triggering time of pulsing tests. A wetting time equal to 0 hour denotes the time that distilled water arrived on the top surface of the specimen through the filter paper. Image color represents the magnitude of transmitted voltage ranging from -1.25 to 2.6 V (red: positive, blue: negative and white: 0 value). Transmitted energy is shown between the bandwidth of 100 kHz to 1 MHz in the frequency domain (Figure 4(b)). The image color indicates the magnitude of the transmitted energy, ranging from -73 to -16 dB (changes in the order of magnitude of 2 to 3). Results of coda waves, selected from 200 to 220 μs of acoustic duration, are presented in the time and frequency domain (Figure 4(c) and 4(d)) and follow a similar color scheme as the direct waves. An immediate reduction in the transmitted energy was observed upon wetting: the color gradually turns lighter when the wetting front is moving downwards through the specimen from the top surface. Amplitude decreases in the attenuated energies of the direct waves, order of magnitude 1 to -1 and coda waves, order of magnitude -1 to -2 were observed and both exhibited $\sim$ 24 dB reduction. This finding is supported by the DIC results that rocks experienced expansion upon wetting in Section 4.2. The acoustic derived changes outlined in the next sections are summarized in Table S1 of the Supporting Information.

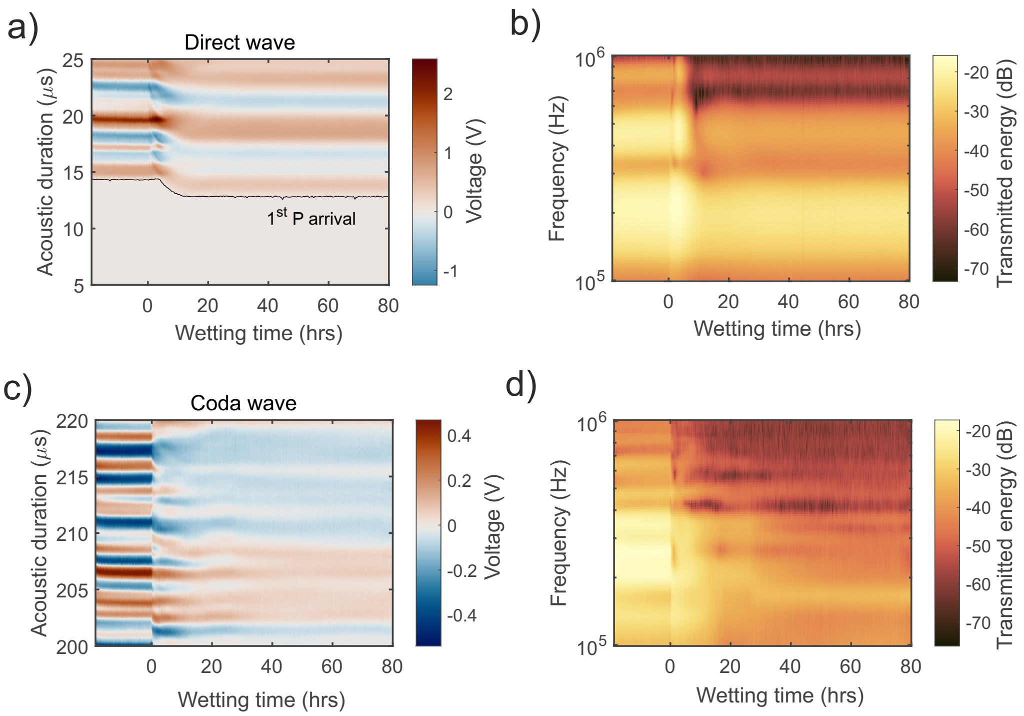

Figure 4. Changes in stacked acoustic waveforms over 98 hours in response to water availability. Direct waves in (a) time domain (acoustic duration: 5 to 25 μs) and (b) frequency domain (frequency bandwidth: 100 kHz to 1 MHz). The onset of the P-wave arrival is shown in black (a) and is illustrated more prominently in Figure 5. Coda waves in (c) time domain (acoustic duration: 200 and 220 μs) and (d) frequency domain (frequency bandwidth: 100 kHz to 1 MHz).

4.1.1 Changes in P-wave phase arrivals

The onset of P waves (black line in Figure 4(a)) progressively decreased from 14.35 to 12.85 μs between 0 to $\sim$ 16 hours. This increase in P-wave velocity (V_p) is due to the imbibition of water. In Figure 5(a), P-wave velocity is initially measured at approximately 4538 $\pm$ 10 m/s, decreases slightly to 4507 m/s from 0 to 3.2 hours, and rises to a plateau (5074 $\pm$ 19 m/s) at approximately 16 hours. The onset of S waves is not included in this study because multiple reflections from the outer boundaries between the P- and S-wave onset mask the first arrival of the S wave.

4.1.2 Changes in transmitted energy of P and coda wave phases

We found that changes in the transmitted energy upon wetting was frequency-dependent. For example, in Figure 4(b), there is a highest energy decrease (> 15 dB) at high frequency (e.g. 900 kHz) and less energy decrease (> 5 dB) at low frequency (e.g. 150 kHz). Figure 5(b) shows transmitted energies averaged at three frequency bandwidths: LF = 100 to 300 kHz, dashed line; MF = 300 to 600 kHz, dotted line; and HF = 600 to 1000 kHz, solid line, for direct (red) and coda (black) waves. Time O (0 hour) is marked as the thick blue line in Figure 5. The subsequent times *i* (1.3 hours), *ii* (3.2 hours), *iii* (9 hours), *iv* (16 hours) and *v* (32 hours) are shown as blue dashed vertical lines and represent the turnings of P-wave velocity and transmitted energy. Changes in the transmitted energy of the P and coda wave phases are denoted as ΔT_d and ΔT_c, respectively.

Prior to time O, specimen remains in a steady state since transmitted energy in direct and coda waves is stable (all variations below 1 dB). Once water is introduced to the top surface of the specimen (time O at 0 hour), ΔT_d increases from time *i* to *ii* (1.3 to 3.2 hours) as the frequency bandwidth changes (ΔT_d^{LF} = + 2.6 dB, ΔT_d^{MF} = + 3 dB and ΔT_d^{HF} = + 4 dB). As the time increases, i.e., *ii* to *iii* (3.2 to 9 hours), ΔT_d begins to decrease as the bandwidths are changed (ΔT_d^{LF} = - 9.0 dB, ΔT_d^{MF} = - 19.5 dB and ΔT_d^{HF} = - 27 dB). After time *iii* (9 hours), ΔT_d starts to recover at all bandwidths (ΔT_d^{LF} = + 0.6 dB, ΔT_d^{MF} = + 5.5 dB and ΔT_d^{HF} = + 8 dB) and stabilizes at time *iv* (18 hours) with a $\pm$ 0.1 dB change over all bandwidths.

The transmitted energy of the coda waves behaves differently from that seen in the direct waves. ΔT_c immediately decays from time O to *i* (0 to 1.3 hours) (ΔT_c^{LF} = - 5 dB, ΔT_c^{MF} = - 5.9 dB, ΔT_c^{HF} = - 7.1 dB). While between *i* and *ii* (1.3 to 3.2 hours), ΔT_c shows

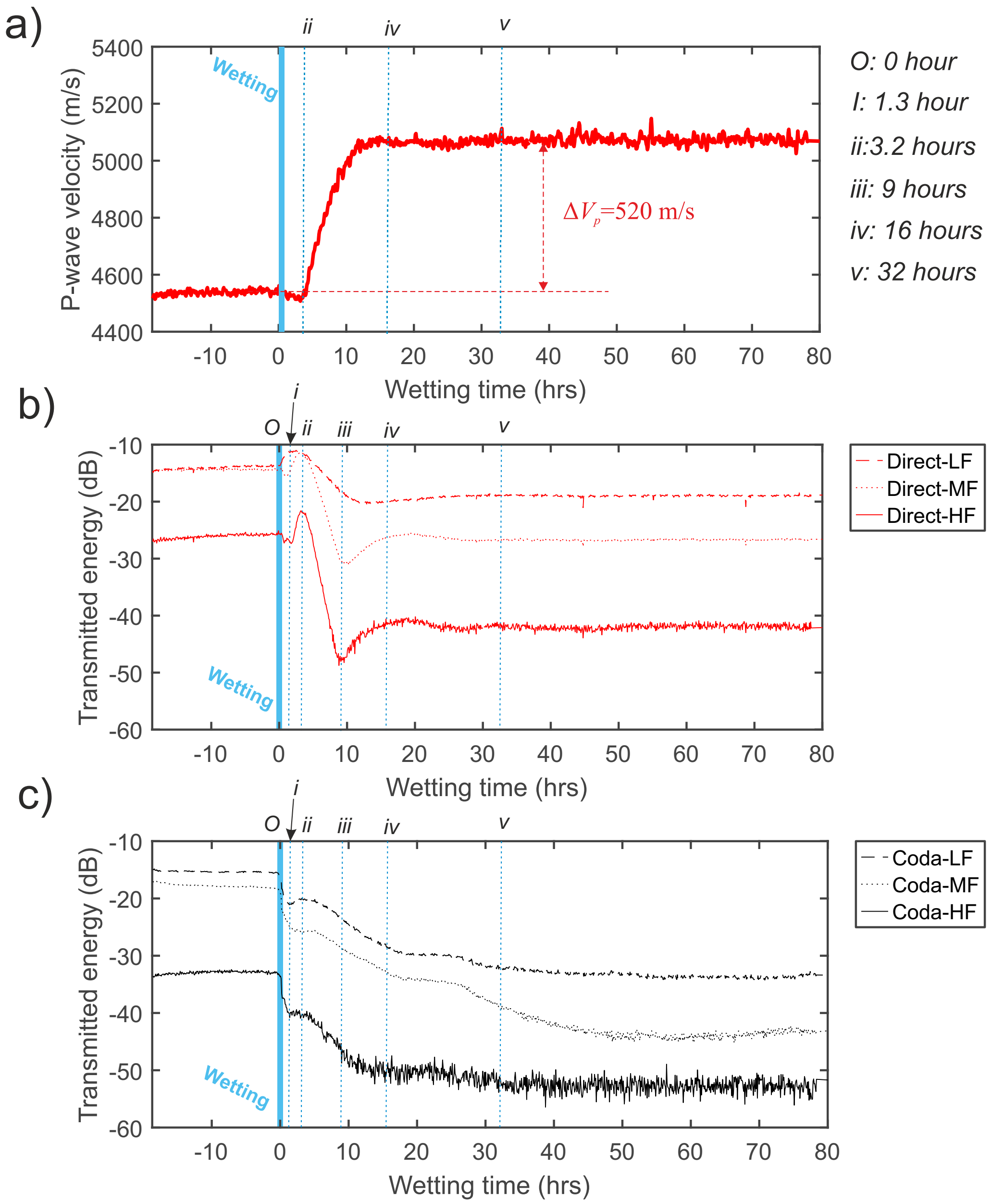

Figure 5. Changes in acoustic signatures over 98 hours in response to water availability. (a) Measured P-wave velocity between 4538 and 5074 m/s. Transmitted energy averaged at three frequency bandwidths (100 to 300 kHz, 300 to 600 kHz, and 600 to 1000 kHz) for direct (b) and coda (c) waves. These frequency bandwidths are denoted as *LF*-low frequency, *MF*-medium frequency, and *HF*-high frequency, respectively. Vertical blue dashed lines indicate a few turning point of transmitted energy and P-wave velocity.

a small rebound at around 1 dB. Afterwards, ΔT_c attenuates until 37 hours (ΔT_c^{LF} = -13 dB), 46 hours (ΔT_c^{MF} = - 19 dB) and 35 hours (ΔT_c^{HF} = - 12.8 dB) and then remains stable (± 0.5 dB).

Throughout the entire wetting stage (0 to 80 hours), the total ΔT_d at different frequencies is - 4.6 dB (*LF*), - 12.6 dB (*MF*), - 17 dB (*HF*) while ΔT_c is - 18 dB (*LF*), - 26.6 dB (*MF*), and - 20 dB (*HF*), respectively.

4.1.3 Changes in P-wave quality factor

Spectral ratio methods (Toksöz et al., 1979) were utilized in this study to characterize seismic wave attenuation of Herrnholz granite independent of frequency. Ultrasonic pulse transmission monitoring were performed using the same procedures that were used in the wetting experiment on Herrnholz granite specimens and a reference material, Aluminum. The Aluminum was used due to its extremely low attenuation with respect to rocks (Zemanek & Rudnick, 1961). The geometry of the Aluminum specimen was identical to the Herrnholz granite specimen shown in Figure 3. The amplitude (A) of plane elastic body waves for the Aluminum (subscript 1) and Herrnholz (subscript 2) specimens can be expressed as:

$$A_1(f) = G_1(x)e^{-\frac{\pi f x}{Q_1 v_1}} e^{i(2\pi f t - k_1 x)}, \tag{2a}$$

$$A_2(f) = G_2(x)e^{-\frac{\pi f x}{Q_2 v_2}} e^{i(2\pi f t - k_2 x)}, \tag{2b}$$

where f and k are the frequency and wavenumber of the received waveforms, v is the P-wave velocity, x is the distance between source and receiver (65 mm) and $G(x)$ is a frequency-independent geometrical factor that includes geometrical spreading and reflections.

P-wave amplitude is cropped from onset to the first zero-crossing (or half wavelength) as shown in Figure 6(a). The P-wave data for the Herrnholz granite is aligned at the triggering time. Before the wetting stage (below 0 hour), P-wave data (grey line) overlap well within 18 hour with a maximum amplitude of 0.7 V. The maximum amplitude increases to $\sim$ 1 V from 0 to 3.2 hours, and then decreases to 0.37 ± 0.1 V until 25 hours (blue: early; yellow: late). P-wave data after 25 hours (light blue) remains stable until the end of the measurement. The duration increases from 2 to 2.5 μs which suggests an increasing loss of high-frequency spectral components. P-wave data from the Aluminum specimen (dashed

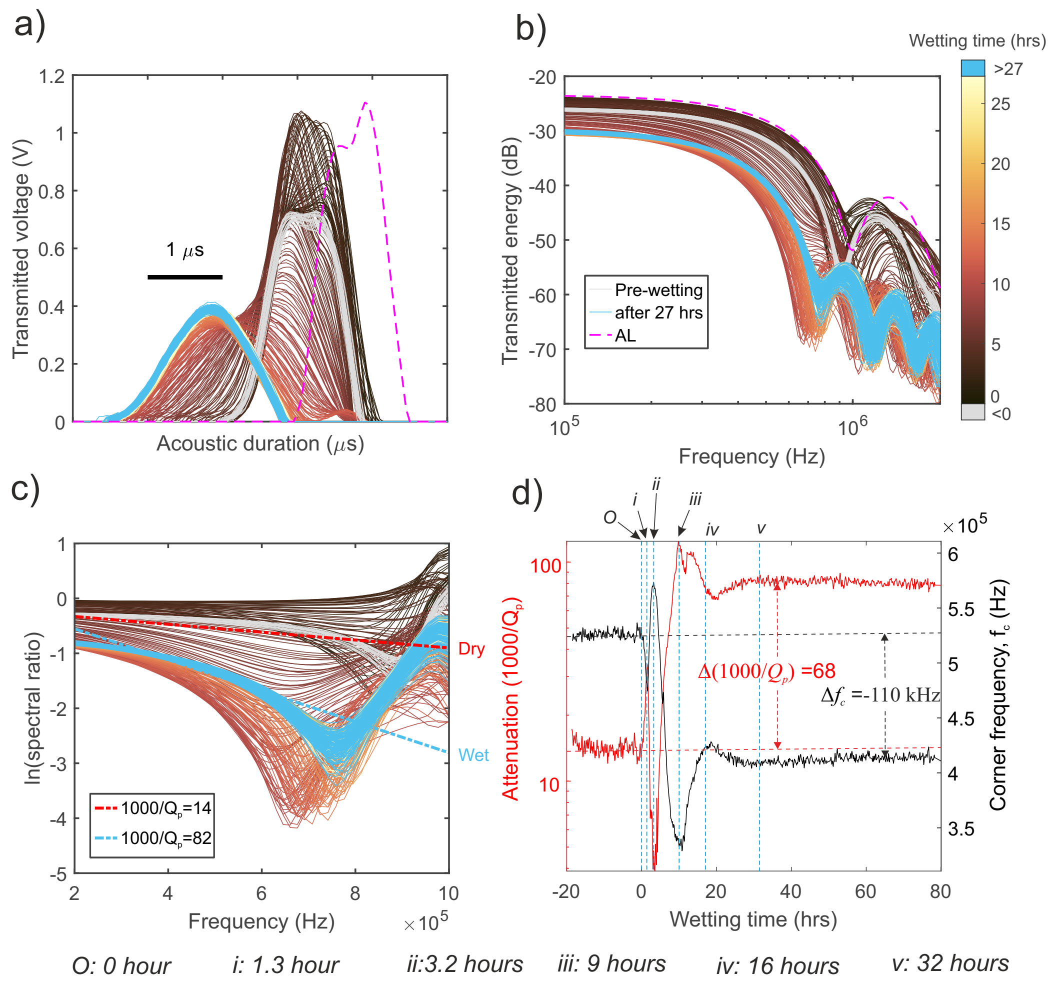

Figure 6. P-wave data from onset to its first zero-crossing in (a) time domain and (b) frequency domain. Grey, blue/yellow and light blue denote the dry, gradual wetting and equilibrium wetting stages of Herrnholz granite. Magenta represents data from the Aluminum specimen. (c) Natural logarithm of the ratio of Herrnholz granite to Aluminum in Fourier amplitudes. The slope is given to show how the P-wave quality factor of the granite specimen, Q_p, evolves from 87 (red dash, dry) to 16 (blue dash, wet). (d) Inverse P-wave quality factor and corner frequency versus wetting time (blue dashed lines indicate some turning points).

magenta line) is also shown but without the alignment of triggering time for visualization purpose. In Figure 6(b), transmitted energy starts to attenuate significantly (> 10 dB) at higher frequencies (e.g. above 500 kHz). the natural logarithm of the spectral ratio of transmitted energy for the Herrnholz granite to Aluminum is given as:

$$\ln\left(\frac{A_1}{A_2}\right) = \left(\frac{1}{Q_1 v_1} - \frac{1}{Q_2 v_2}\right)\pi x f + \ln\left(\frac{G_1}{G_2}\right) \quad (3)$$

and is shown in Figure 6(c). $1/Q_i$ $(i = 1, 2)$ is the inverse quality factor of the direct P-wave phase. $1/Q_i$ could be simply stated as the percentage loss of carried energy in the direct P-wave phase where a high value denotes high attenuation, and vice versa. The term $\left(\frac{1}{Q_1 v_1} - \frac{1}{Q_2 v_2}\right)$ can be found from the slope of the line fitted to $\ln\left(\frac{A_1}{A_2}\right)$ because $\frac{G_1}{G_2}$ is independent of frequency. Q_2 (Aluminum) is extremely high (about 1.5 x 10^5 from Zemanek and Rudnick (1961)) compared to that for rocks (tens to hundreds) so that the term $\frac{1}{Q_2 v_2}$ is ignored. Q_1, which represents the Q_p of Herrnholz granite, was derived using the variation in P-wave velocity as the water content increased.

In Figure 6(d), prior to introducing water, $1000/Q_p$ (14 ± 1.5) remains stable. As the specimen gradually becomes wetter, $1000/Q_p$ increases by 20 up to time *i* at 1.3 hours, decreases by 4 at time *ii* (3.2 hours), increases by 120 until it reaches time *iii* at 9 hours, and slowly decreases to 87 by the time it reaches time *iv* at 16 hours. After time *iv*, little variations is observed in $1000/Q_p$ (82 ± 3).

4.1.4 Changes in corner frequency

It has been suggested that the characteristic frequency of transmitted energy is correlated to the stiffness changes in elastic objects (Christaras et al., 1994; Burjánek et al., 2017; Moore et al., 2018). When the geometry of an object remains constant, the characteristic frequency can be related to the stiffness and vice versa. In our study, since a non-resonant PZT actuator and receiver were used (see Section 3.3), the corner frequency of studied spectra was used instead of the resonant frequency and is denoted as f_c. We used the *Omega-n* model (Hanks, 1979) to perform spectral fitting of transmitted energy outlined in Wu et al. (2021, see equation (21)) so that f_c was obtained. In Figure 6(d), it can observed that variations in f_c (black) are opposite to $1000/Q_p$ (red). Before time *O*, the corner frequency (525 ± 5 kHz) remains stable. When water is introduced to the top surface of the specimen, the corner frequency decreases by 51 kHz until time *i* at 1.3 hours, increases by 99 kHz until time *ii* at 3.2 hours, decreases by 243 until time *iii* at 9 hours and then slowly increases by 86 until time *iv* at 16 hours. After 16 hours, little variations was observed in f_c (412 $\pm$ 6 kHz).

4.2 Moisture-induced surface deformation

Using the DIC methods, (Li et al., 2021) analyzed 744 images over 98 hours and observed extensional strains in both the horizontal (x) and vertical (y) directions. The vertical expansion particularly provided an useful insight of the moving wetting front. We here similarly use the contour line ($= \times 10^{-4}$, indicated by the white dashed line) of the vertical strain to track the infiltration front in Figure 7. We presented vertical strain fields from time i to v which were turnings of acoustic attributes previously defined in Section 4.1. We found the wetting front reached approximately $y = \sim 9$ mm by time i or 1.3 hours (Figure 7(a)), $\sim$ 11 at time ii or 3.2 hours (Figure 7(b)), $\sim$ 17.5 mm at 7 hours (Figure 7(c)), 20.5 mm at time iii or 9 hours (Figure 7(d)), and 28 mm at time iv or 16 hours (Figure 7(e)). The vertical strain front (ϵ_{yy}) progressed past the ROI (region of interest) at time v or 32 hours in Figure 7(f); the magnitude of vertical strain was $\sim 10^{-4}$ over the entire ROI at this time. Peaks in the vertical strain field between $10 - 20 \times 10^{-4}$ were observed around the upper edge of ROI and they decreased below 5×10^{-4} at $y = \sim 9$ mm. In Figure 7(a), three dark blue patches can be observed in the top of the ROI, which corresponds to the location of the three aluminum blocks placed on the filter paper. We believe this results in a slightly heterogeneous distribution of the water on the top surface of the contact regions.

When infiltration reached 16 hours, ahead of wetting front, water vapor or a small amount of liquid water intrusion into the local heterogeneities (such as microcracks) caused extension in few small patches ($\sim$ 10 mm $\times$ 5 mm) with strains of $\sim$ 0.8 to 1×10^{-4} (see Figure 7(e)). This is also supported by the observation at 32 hours: the wetting front evolves slightly non-uniformly from left to right. The position of the ultrasonic monitoring pair is installed 20 mm below the wetting surface and the correlation between surface strain and acoustic changes will be discussed in Section 5.2. Results for the horizontal strain at the same six time intervals are provided in Figure S1 of the Supporting Information to give a tabular summary of the expansion process.

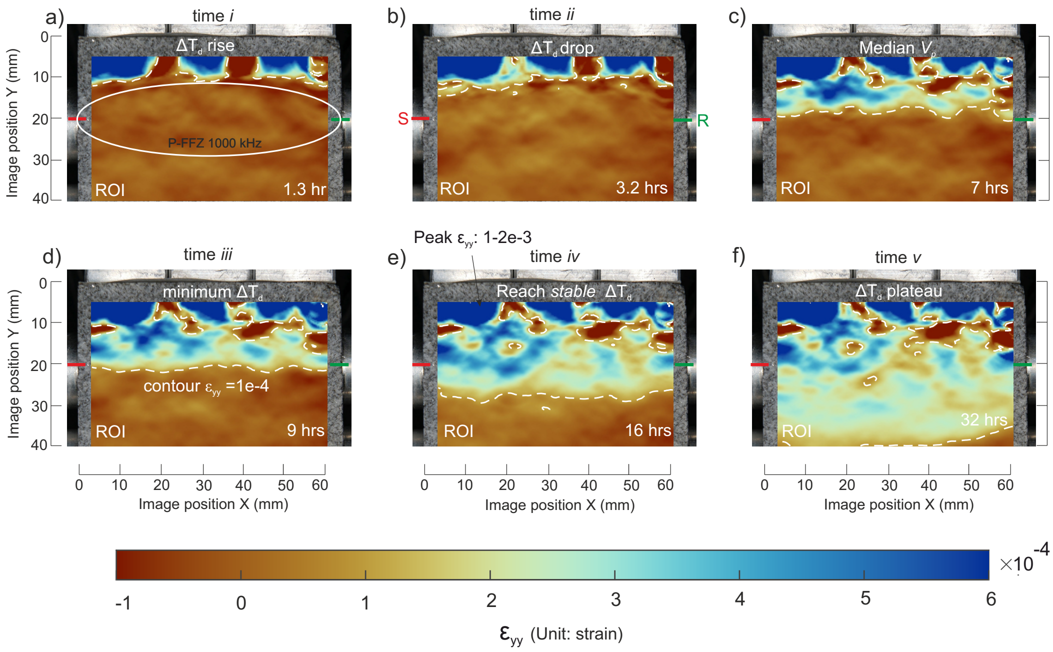

Figure 7. Vertical strain (ϵ_{yy}) evolution on the front surface of the granite specimen (ROI: 65 mm in width and 40 mm in height) as water is applied. Wetting time equal to 0 hour denotes the start of water application to the top surface of the specimen. Times *i* to *v* are the times previously defined in the acoustic signature analysis.

5 Discussion

5.1 Observed ΔV_p in nanopores in response to water infiltration

P-wave velocity changes, ΔV_p, observed in the free-standing progressive wetting test are discussed here. Prior to introducing water, there was less than a 0.1 % fluctuation in ΔV_p which indicates stable ambient environmental conditions. When water is introduced to the top surface of the specimen at time O or 0 hour, the P-wave velocity decreased slightly by 0.5 % until time *ii*. This apparent elastic weakening could be attributed to moisture adsorption at lower saturation level S_w. Water vapor ahead of the liquid water might coat the dry walls of grain contacts in the form of monolayers or condense to liquid phase. The both effects could reduce the contact stiffness of the grain through the reduction of free surface energy and generation of capillary pressure (Gor & Neimark, 2010; Gor & Bernstein, 2016; Gor et al., 2017; Yurikov et al., 2018; Li et al., 2021). Similar elastic weakening in rocks with different microstructures has been observed at laboratory ultrasonic frequencies (Murphy III, 1982). For clay-deficient rocks, P-wave velocity decreases by less than 20 % until S_w reaches 0.5 % in quartz-pure sandstone (Pimienta et al., 2014), by 4 % until S_w reaches 10 % (Cadoret et al., 1995) in limestone and 0.5 % until S_w is 2.5 % in limestone (Pimienta et al., 2014). The elastic weakening that is partially caused by clay swelling (Yurikov et al., 2018, 2019; Tiennot & Fortin, 2020) is outside the scope of this study.

P-wave velocity dispersion was observed as ΔV_p increased by 520 m/s from time *ii* to *iv*. From the vertical strain evolution shown in Figure 7(b) to (e), the wetting region is almost symmetrical around the source-receiver straight ray path and overlaps with the P-wave first Fresnel zone (P-FFZ). The minor radius size of the P-FFZ, R_1, will be discussed in Section 5.2.2. After time *iv*, the wetting front fully passed P-FFZ (Figure 7(f)), ΔV_p stabilized with less than a 2 % variation over tens of hours. This indicates that a stable equilibrium has been reached between water wetting in the interior of the specimen and evaporation through the specimen's surfaces.

5.1.1 *Squirt flow or Gassmann theory in microcracked nanopore-dominated media?*

We modeled P-wave velocity dispersion in saturated Herrnholz granite within the context of classic theories of fluid substitution in porous media. Gassmann theory was validated at sufficiently low frequency (e.g. *in situ* seismic monitoring below 100 Hz and sonic logging below tens of kHz) at which fluid pressures gradients within interconnected pores, induced by elastic waves, can be dissipated within sufficient time (Mavko et al., 2020, Section 6.3). To extend the Gassmann theory to laboratory ultrasonic frequency (hundreds of kHz to few MHz), the average pore size ($\hat{d}$) must be much smaller than the viscous skin depth $\delta = (\eta/\pi f \rho_{\mathrm{f}})^{1/2}$ (Biot, 1956; Johnson et al., 1987; Gor & Gurevich, 2018). η and ρ_f represent the dynamic fluid viscosity (unit: $Pa \cdot s$) and density of the saturating fluid (distilled water) (units: g/cm^3), respectively, and f is the ultrasonic resonant frequency. Table 1 summarises the essential input parameters (e.g. density, modulus, porosity, frequency) from the water-accessible porosity measurement (Section 2.2) and elastic piezosensitivity analysis (Section 2.4). We find that the assumption of Gassmann theory is satisfied (Johnson et al., 1987) because $\hat{d} = 10\ nm \ll \delta = 546\ nm$.

Table 1. Parameters for P-wave velocity dispersion modeling in Herrnholz granite.

Water	K_f (GPa)	$\rho_f (g/cm^3)$	$\eta (Pa \cdot s)$		
	2.2	1	9.4×10^{-4}		
Dry rock	K_{gr} (GPa)	$\rho\ (g/cm^3)$	G_{gr} (GPa)	ϕ_s (%)	
	50.6	2640	30.3	1.54	
Piezo	K_{grs} (GPa)	G_{grs} (GPa)	ϕ_{c0} (%)	α	f (MHz)
	50.4	30	0.071	1.1×10^{-3}	1

Parameters from water-accessible porosity measurement (Section 2.2) and elastic piezosensitivity analysis (Section 2.4).

In Figure 8, we further examine the applicability of the Gassmann theory to P-wave dispersion in intact rocks. The P-wave velocity offset between Gassmann prediction (*Gass*, gray) and laboratory measurement (*Sat*, blue) for the saturated granite specimen is greater at low effective stress (280 m/s at 5 MPa) and then decreases approaching 0 m/s, until the maximum effective stress (79 m/s at 160 MPa). This suggests that Gassmann theory does not fully capture the physics at this scale. By comparing the microstructural differences in nanoporous Vycor glass (Levitz et al., 1991; Gor & Gurevich, 2018) and Herrnholz granite, the effects of natural microcrack characteristics of brittle rocks might contribute to this mismatch.

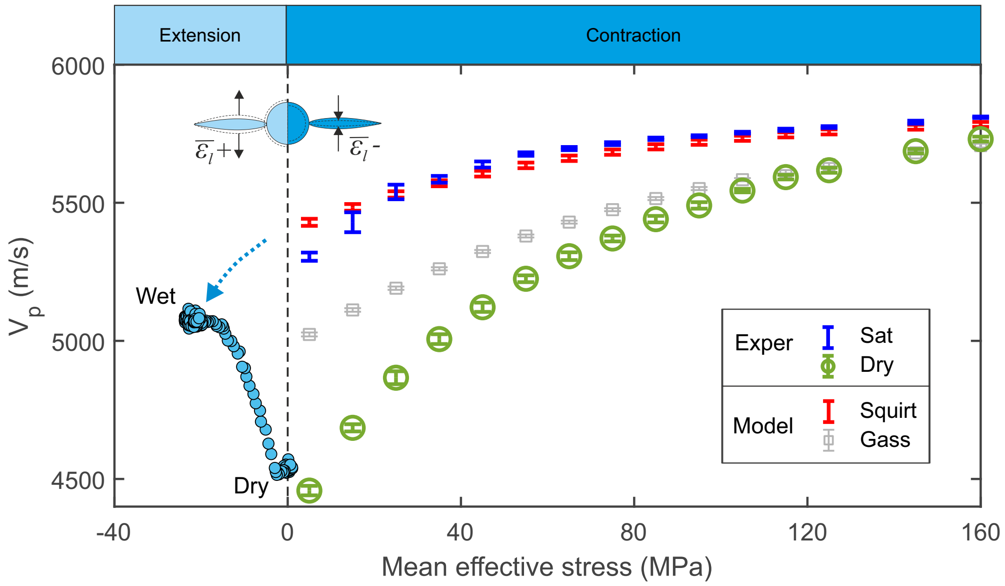

Figure 8. Broadband V_p dispersion in Herrnholz granite under extensional (left) and contractional (right) stress regimes. Left: V_p evolution from *dry* to *wet* measured in the water imbibition test; Right: V_p measured and modeled in the hydrostatic compression test. *dry* (green, experimentally measured), *Sat* or saturated (blue, experimentally measured), *Gass* or Gassmann theory (gray, model prediction) and *Squirt* or squirt flow theory (red, model prediction).

Mavko and Jizba (1991) quantified the effect of compliant pore spaces or microcracks on elastic stiffening in saturated porous media. This is usually referred to the Mavko–Jizba squirt flow theory. The entire pore space is partitioned into a few subsets of stiff and compliant spaces. Compliant pore spaces are presumed to be thin cracks and grain contacts. At sufficiently high effective stress, most of this soft pore space can be compressed to close, or at least be substantially reduced in volume. The stiffness difference between the measurements and Gassmann theory could then be expected to be the result of the unrelaxed/undissipated pore pressure inside the microcracks that resists deformation imposed by the passage of elastic waves. Gurevich et al. (2010) extended this work to a broader frequency range by considering fluid pressure relaxation in penny-shaped gaps between adjacent grains. They inferred that V_p is exactly consistent with the Gassmann theory at a low-frequency limit and transitions to the Mavko–Jizba squirt flow at a high-frequency limit. Parameters for the squirt flow model used here are provided in Table 1.

To test the validity of squirt flow model, we compared the predicted V_p from the squirt flow model (*Squirt*, red) at 1 MHz (resonant frequency of the ultrasonic source-receiver pair) and laboratory measurement (*Sat*, blue) for the saturated granite specimen in Figure 8. In general, the error is less than 0.8 % of measured V_p indicating this model is capturing the observed physics. An anomalous V_p offset of 125 m/s between the *Squirt* and *Sat* at 5 MPa could indicate a contact problem between the granite specimen and adjacent source-receiver pair at a low confining pressure. As the effective stress increases, the error between observed and modelled V_p remains below 40 m/s (0.8 % of measured V_p) and the V_p from squirt flow model correlates well with the V_p changes with confinement for the saturated specimen. While the Gassmann theory works well in nanoporous materials as having stiff pore spaces (e.g. Vycor glass) (Levitz et al., 1991; Gor & Gurevich, 2018), we conclude that P-wave velocity dispersion in water-saturated microcracked nanopore-dominated media can be better modeled using the squirt flow theory.

5.1.2 ΔV_p in granite under extensional and contractional stress regimes

After testing the validity of the squirt flow theory in the tested granite, we then studied V_p dispersion under both extensional and contractional stress regimes. Hygroscopic expansion occurs in the water imbibition test (see Section 4.2) as is assumed to be a result of generation of adsorption stress (also known as solvation pressure) through adhesion and capillary condensation by Li et al. (2021). They estimated this adsorption stress by multiplying the mean hygroscopic strains (denoted as $\overline{\epsilon_l}$) by the pore-load modulus M_{pl} that quantified the deformability of porous media in response to changes in pore fluid pressure (Gor & Neimark, 2010; Yurikov et al., 2018; Gor & Gurevich, 2018): $\sigma_s = M_{pl}$.

The pore-load modulus M_{pl} was assumed to be independent of the gradually wetting process controlled by hydroscopic expansion and was given as $M_{pl} = \frac{3}{1/K - 1/K_{drs}}$. K is the drained bulk modulus of the granite and the static modulus was measured independently to be 18.8 GPa at 20 % RH by Li et al. (2021). The bulk modulus of the granite without pore space, $K_{drs} = 50.4$ GPa, was determined in Section 2.4. M_{pl} is estimated to be 90 GPa and thus the solvation pressure is derived as a function of $\overline{\epsilon_l}$. Li et al. (2021) suggested the mean hygroscopic strain can be given as $\overline{\epsilon_l} = (2\epsilon_{xx} + \epsilon_{yy})/3$, where ϵ_{xx} and ϵ_{yy} are average horizontal and vertical strains within a rectangular region symmetrical around the source-receiver pair. The dimension of this region is 65 mm × 20 mm. More details about this region will be discussed in Section 5.2.2.

To maintain consistency in the contractional condition, mean effective stress $\bar{\sigma}_e$ is adopted instead of solvation pressure (σ_s) by considering $\bar{\sigma}_e = -\sigma_s$ in the case of a free-standing specimen where the specimen is subjected to a zero external stress state. Changes in P-wave velocity and the calculated solvation pressure from the water imbibition test are shown as solid blue circles on the left side in Figure 8. When the specimen saturation changes from ambient humidity conditions (around 20 %) to proressive wetting, V_p and $\Delta\sigma_s$ increase by 520 m/s and 23.6 MPa, respectively. V_p at 0 MPa in the water imbibition test is slightly higher (60 m/s) than V_p at 5 MPa in the hydrostatic compression test. This slight discrepancy was because the ultrasonic monitoring required $\sim$ 5 MPa of confining pressure to generate a proper bond at the contact surface. The steady *Wet* V_p at 23.6 MPa in the water imbibition test could serve as the bound constraint of V_p in the saturated granite at the same $\bar{\sigma}_e$. Following the blue dash arrow in Figure 8, it is possible that the changes seen in V_p between *Wet* and *Sat* V_p could be explained by that squirt flow theory. This may indicate the squirt flow theory is also valid for extensional stress regimes, but this requires more validation work. The observed consistency in V_p between *Wet* and *Sat* provides a straightforward understanding of P-wave velocity dispersion in water-saturated microcracked nanopore-dominated media spanning stress regimes in both contraction and extension.

5.2 Variations in transmitted energy due to water imbibition

Our results indicate that the squirt flow mechanism can account for P-wave velocity dispersion in nanopore-dominated granite, and could also be one of the major causes of seismic attenuation of passing elastic waves. In this section, changes in the transmitted energy of the direct P and coda waves at high frequency are investigated and correlated with simultaneous surface deformations. We found that the transmitted energies at relatively high frequencies are much more sensitive to the approach of a wetting front than at low frequencies (see Figure 5(b)). As a result, we focus attenuation on the high-frequency transmitted energy changes for the direct waves ΔT_d (orange solid line) and coda waves ΔT_c (black dash line) between 600 to 1000 kHz, shown in Figure 9. Imaged strain is averaged within a rectangular box *S1* with dimensions of 60 ×30 mm that is symmetrical along the source-receiver straight ray path. ΔT_d and ΔT_c are correlated with imaged strain evolution (left: horizontal or ϵ_{xx}, right: vertical or or ϵ_{yy}). Times O to v, delineated by the vertical dashed lines, correspond to the same times given in Section 4.1.

5.2.1 Coda wave: ΔT_c

Our results indicate that the transmitted energy, ΔT_c, in coda waves decreases almost instantly with the addition of water at time O by -3.3 dB after 0.5 hour with unremarkable strain variation (below 1.5×10^{-5}). This could indicate coda waves are relatively sensitive to moisture changes in the top boundary of the specimen. An increasing amount of coda energy with time is adsorbed along the wetting boundary instead of reflected to the receiver below. A similar spontaneous decrease of transmitted coda energies was also observed in other water imbibition experiments (Wulff & Mjaaland, 2002; Barton, 2006; David, Barnes, et al., 2017; Pimienta et al., 2019; Thery et al., 2020). As the wetting region progressively expands, the mean ϵ_{xx} and ϵ_{yy} are found to monotonously increase from 0 to 2.8×10^{-4} and 0 to 3×10^{-4} , respectively, until time v. This has been associated with the adsorption-induced deformation of the tested material (Li et al., 2021). As the specimen expanded, we noticed a continual drop in ΔT_c, which decreased at a relatively constant slope until time v. The wavelength of the excited elastic waves ranged from 4.5 to 8.5 mm and is much smaller than the specimen size. Local heterogeneities have been shown to cause more scattering and adsorb more energy during elastic wave propagation (Aki & Chouet, 1975). The decaying rate of ΔT_c is also lower than that during first 0.5 hours and this could be attributed to the wetting rate difference between the lateral and top surfaces.

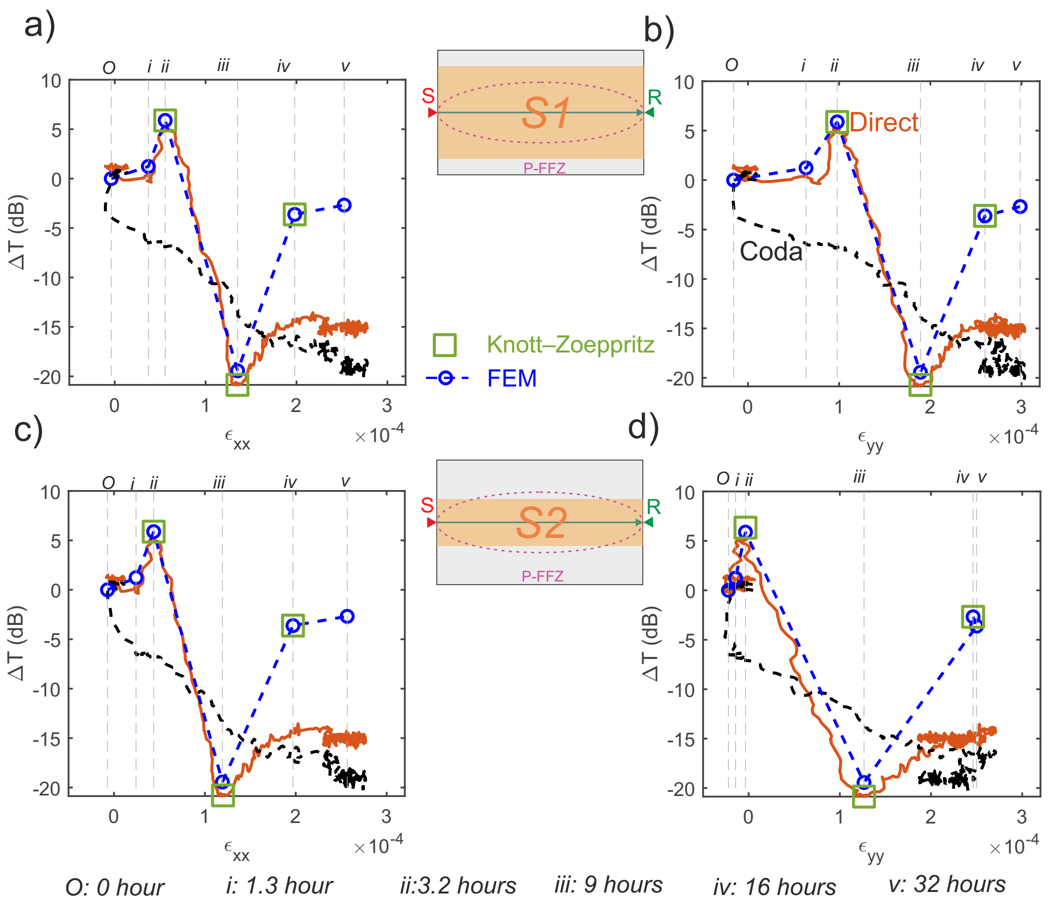

Figure 9. Experimentally measured transmitted energy (direct wave: orange solid line, coda wave: black dashed line) evolution with imaged strain (left: horizontal or ϵ_{xx}, right: vertical or or ϵ_{yy})). Strain is averaged within box *S1* for a) and b), and box *S2* for c) and d), respectively. Blue circles denote numerical analysis introduced in Section 5 of the Supporting Information. Vertical grey dashed lines denote times *O* to *v* that were previously defined in acoustic signature analysis.

5.2.2 Direct P wave: ΔT_d

The transmitted energy in direct P waves, ΔT_d, behaves differently from that of coda waves throughout the wetting experiment. A peculiar observation was made with ΔT_d after the initial introduction of the water to the specimen. ΔT_d initially remained stable until time i when the wetting front was inside box *S1*. The theoretical R_1 of P-FFZ gives 11.3 mm at 600 kHz and 8.7 mm at 1000 kHz, respectively (equation (1)). Comparing the relative position of wetting front and P-FFZ, the ΔT_d plateau remains because the direct P-wave phase mirrors the elastic changes within the P-FFZ. The ΔT_d plateau is followed by a small increase from 0 dB at time i to 5.2 dB at time ii. A similar increase was also observed in the P-wave amplitude (first peak) in water imbibition experiments on Sherwood sandstone (mean pore throat diameter of 18 μm, see David, Barnes, et al. (2017)). Since the squirt flow mechanism only accounts for seismic attenuation, there should exist another mechanism for seismic amplification.

5.2.3 Analytical solution of plane wave propagation to explain ΔT_d

We aim to provide an explanation for the increase in ΔT_d starting from elastic wave propagation and reflection between wetting front and incident P waves in P-FFZ. We adopt a similar explanation to that provided by Kovalyshen (2018) where the varying moisture conditions changes the material properties and contributes to the presence of a distinct layer in the medium. We suggest this layer occurs at the wetting front and has properties of both the dry and wet granite across this heterogeneity. This layer is assumed to be ideally flat and sharp and represent the solid-solid interface of the fully saturated (above) and dry (below) regions. The point source and receiver are assumed to generate and receive elastic waves. For the wetting phase, $\rho = 2.64\ g/cm^3, V_p = 4550\ m/s$ and $V_s = 2750\ m/s$. For the dry phase, $\rho = 2.649\ g/cm^3, V_p = 5300\ m/s$ and $V_s = 2850\ m/s$ (measured data from a hydrostatic compression test). In Figure 10(a), the wetting front is located above the source-receiver straight ray path. Depending on the incident angle θ, incident P waves could arrive at the receiver directly along the shortest path, i.e., $\theta = 90°$, along the green solid line. At $\theta < 90°$, incident P waves along the green dashed line will reflect on the interface, convert into reflected P (denoted as Pp) and S (denoted as Ps) waves and arrive at the receiver with a time delay from the direct P waves. We adopt the same nomenclature as Kovalyshen (2018).

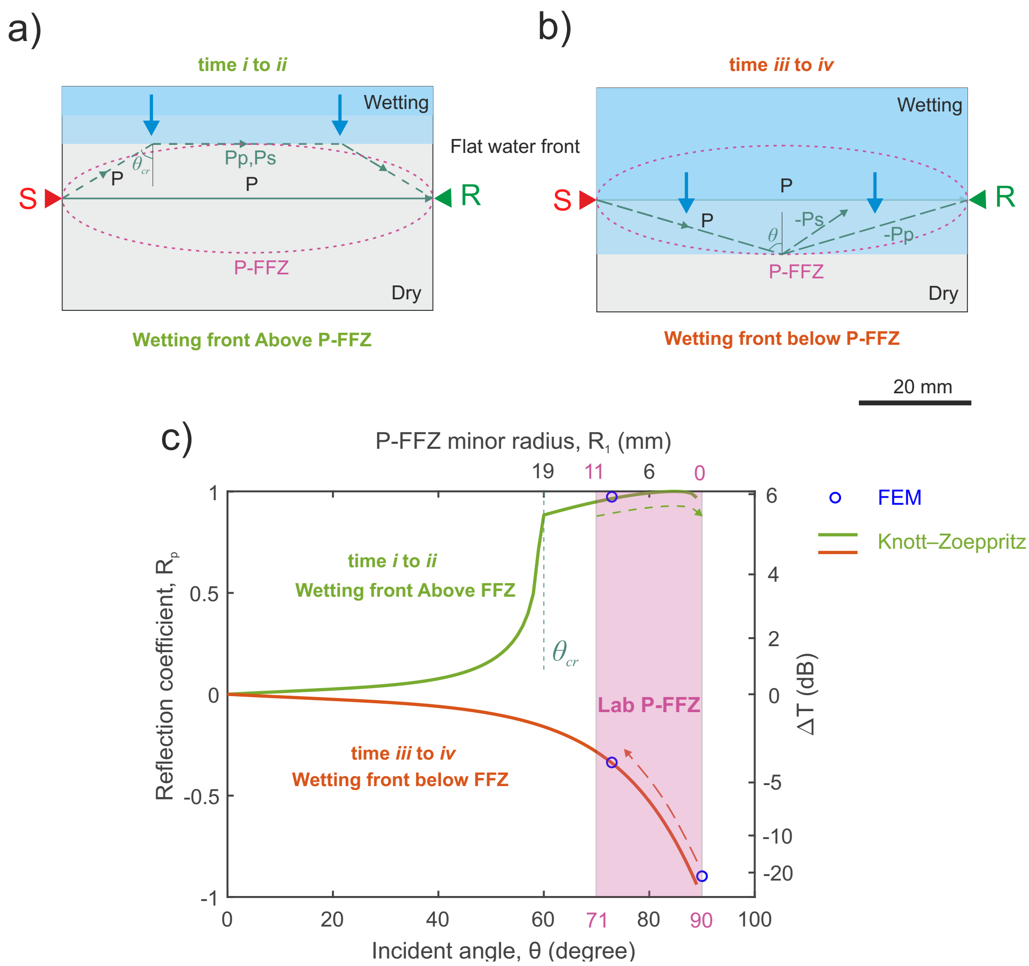

Figure 10. Propagation and reflection of incident P waves on the wetting front. a) Wetting front migrates from the top surface of the specimen to interact with the top co-vertex of the P-FFZ. b) Wetting front moves from the source-receiver straight ray path to the bottom co-vertex of the P-FFZ. The corresponding reflection coefficient R_p in a) and b) is solved using the Knott–Zoeppritz equation (solid lines) and FEM modeling (blue circles, introduced in Section 5 of the Supporting Information). The pink shaded area denotes the minor radius range R_1 of the laboratory P-FFZ.

We present the complete solution (green line) of the incident plane P-wave reflection coefficient R_p on the solid-solid interface, solved using Knott-Zoeppritz equations (Mavko et al., 2020, Section 3.5) in Figure 10(c). Unit conversion between R_p (left y-axis) and ΔT_d (right y-axis) is give as $\Delta T_d = 20\log_{10}(1 + R_p)$. A turning point of 60° denotes the grazing angle beyond which total internal reflection occurs with R_p close to 1. When the wetting front arrives the top co-vertex of 600 kHz P-FFZ at $R_1 \approx 11$ mm or $\theta \approx 71°$, reflected P and S waves start to affect the initial direct P wave and enhance the amplitude with synthetic waveforms. From time *i* to *ii*, the wetting front continuously moves downwards with a vertical distance away from the source-receiver straight ray path from an averaged 11 mm to an averaged 9 mm. This observation matches well with the theoretical R_1 of P-FFZ, which is 11.3 mm for 600 kHz and 8.7 mm for 1000 kHz. The slight difference could be due to the definition of the dry/wet region (strain below and above 1×10^{-4}), position estimate of the non-uniform wetting front, the gap between experimental and ideal conditions (e.g. finite-dimension specimen, water-induced heterogeneity). Simultaneous monitoring of acoustic and DIC imaging effectively constrains the P-FFZ size which has allowed us to develop a model to better describe these observations. We conclude that from time *i* to *ii*, the wetting front continuously interacts with the P-FFZ, characterised by the frequency increasing from 600 kHz. The experimentally observed ΔT_d is enhanced by 5.2 dB, compared to the theoretical estimate of 5.8 dB shown in Figure 10(c).

Proper correlation of transmitted energy changes with surface deformation needs an understanding of the physics occurring in the same region. Inconsistent variation between ΔT_d and ϵ_{xx} or ϵ_{yy} from time *O* to *i* originates from the size difference between the DIC ROI and P-FFZ. This motivated us to use another rectangular box *S2* (dimension: 60 ×16 mm) as the new DIC ROI where the averaged ϵ_{xx} and ϵ_{yy} within *S2* are shown in Figure 9(c) and (d). At time *O*, *i* and *ii* (with a similar finding in time *iv* and *v*) there is almost the same strain, which suggests an acceptable overlap between the DIC ROI (box) and F-PPZ (ellipse). From time *ii* to *iii*, the wetting front enters all P-FFZs between 600 to 1000 kHz. ΔT_d decreases relatively linearly with the imaged strain until the maximum attenuation of -20.8 dB is reached. At time *iii*, the wetting front slightly surpasses the position of the source-receiver straight ray path and the amplitude sign of reflected P and S waves will be opposite to the direct P wave with a phase shift of 180° as shown in Figure 10(b). No total internal reflection occurs. The theoretical estimation of ΔT_d is given as -20.9 dB at $\theta \approx 88.5°$, compared to the experimental observation of -20.8 dB.

Once the wetting front passes the source-receiver straight ray path, ΔT_d recovers after time *iii*. ΔT_d remains at -15 dB with 0.5 dB variation at time *iv* when the wetting front leaves the P-FFZ. No similar recovery is found in the coda waves. The orange line in Figure 10(c) is the Knott-Zoeppritz solution, and shows R_p that slowly recovers from -24 dB at $\theta \approx 89°$ ($R_1 \approx 0$ mm) to -3.6 dB at $\theta \approx 71°$.

The difference between experimental observations (-15 dB) and the theoretical estimations (-3.6 dB) could originate from hygroscopic expansion and squirt flow. Hygroscopic expansion due to water infiltration occurs and reaches a a mean extensional strain of 2.6×10^{-4} within *S2*. This induces an internal solvation pressure of 23.6 MPa. Hygroscopic expansion reduces the effective normal stress (0 to -23.6 MPa, where minus denotes extension) across the contact area of microcracks filled with water. Less acoustic energy is transmitted through the weakly contacted microstructure. When elastic stress waves pass the saturated region, the microcracks are compressed and local pressure gradients are created. We suggest the pore fluid absorbed along the microcracks will squirt into stiff pores against internal friction so that the transmitted energy is partly transformed into heat energy. It has been previously noted that the squirt flow dominates at zero effective stress and almost disappears when microcracks close (Mavko & Jizba, 1991; Gurevich et al., 2010); hygroscopic expansion can be expected to increase pore aperture, and therefore enhance the squirt flow effect, resulting in higher ΔT_d. The combined effects of squirt flow and hygroscopic expansion will decrease the ΔT_d.

5.3 Corner frequency shift of direct P waves due to water imbibition

In this section we discuss the corner frequency shift of the direct P waves as the wetting front approaches. Since we observed opposing trends in P-wave inverse quality factor $1000/Q_p$ and corner frequency f_c (see Section 4.1.4), we assume that the observed f_c shift might be caused by the same mechanism as $1000/Q_p$ – propagation and reflection of incident P waves around the wetting front around P-FFZ.

The Knott-Zoeppritz theories (Mavko et al., 2020, Section 3.5) do not allow for changes in corner frequency of received waveforms. We also noticed the discrepancy between the plane P-wave assumption in the Knott-Zoeppritz equations and the realistic (3D) elastic wave propagation in our experiments. We developed a full 3D FEM model of elastic wave propagation and reflection in the two-layered medium (see Figure 10), adopting the same parameters (e.g. density, P-wave and S-wave velocity) introduced in Section 5.2.3. The modelling methodology and results, including numerical waveforms in both the time and frequency domain, are presented in Section 5 of the Supporting Information.

The corner frequencies of synthesized numerical waveforms were calculated at different times following the same procedures in Section 4.1.4. To validate the ability of our FEM to explain the f_c shift due to water imbibition, we compared corner frequencies from experimental measurements (purple solid lines) and numerical analysis (blue circles) in Figure 11. Corner frequencies were correlated with simultaneous strain ϵ_{xx} (left) and ϵ_{yy} (right) averaged within box *S2*.

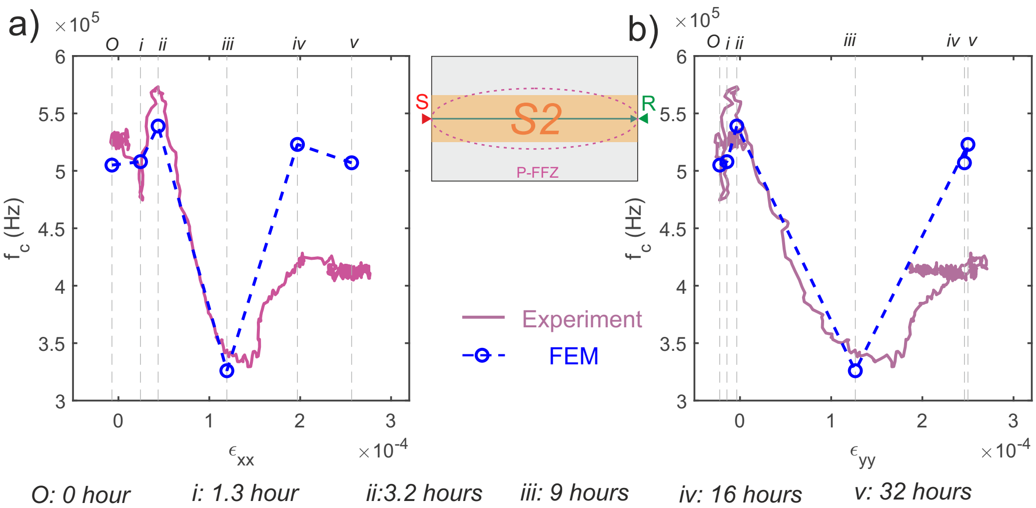

Figure 11. Corner frequency of direct P wave evolution with imaged strain (left: horizontal or ϵ_{xx}, right: vertical or or ϵ_{yy}). The purple solid line denotes experimental measurements and the blue circles are results from the numerical analysis introduced in Section 5 of the Supporting Information. Strain is averaged within box *S2*. Vertical grey dashed lines denote time *O* to *v* that were defined previously in the acoustic signature analysis.

At times *O*, *i*, *ii* and *iii*, the corner frequencies from experimental measurements and numerical analysis are relatively close, with less than 30 kHz offset. This suggests that the previous analysis on elastic wave propagation and reflection in the two-layered medium separated by a wetting front, can really explain observed corner frequency shift. The corner frequency shift is mainly due to the waveform synthesized from incident P and reflected waves. When the water adsorption of porous materials around and within the P-FFZ reaches equilibrium, corner frequencies from the numerical analysis diverges from that of the observed experimental results. The experimentally measured f_c decreases by around 110 kHz while the FEM-derived f_c fully recovers to that of a dry status.

This divergence is reasonable since the FEM modeling was performed within the framework of linear elastodynamics and varying elastic properties due to hygroscopic expansion may also contribute to the change of corner frequency. Li et al. (2022) evaluated the elastic properties of Herrnholz granite subjected to uniaxial compression by increasing RH from 20 % to 90 %. They found a progressive accumulation of volumetric strain up to 8.4×10^{-4}, along with a decrease in Young's modulus from 43 GPa to 38 GPa, and an increase in Poisson's ratio from 0.12 to 0.26 across this RH range. The observed elastic weakening due to hygroscopic expansion is not modeled in this study. We conclude that the corner frequency changes that occurs before reaching the evaporation/adsorption equilibrium are mainly caused by elastic wave reflection when the wetting front is within the P-FFZ; later, the corner frequency changes occurs due to other mechanisms (e.g. adsorption-induced elastic weakening).

6 Conclusions

Realizing the gap in the understanding of elastic variations between macropores and nanopores in microcracked media, we quantified moisture-induced elastic changes in intact Herrnholz granite, a microcracked nanopore-dominated medium, through a laboratory time-lapse acousto-mechanical study. Changes in P-wave velocity, acoustic energy, and corner frequency were examined over 98 hours utilizing time-lapse ultrasonic monitoring. Simultaneous digital image correlation was performed to track the wetting front in real-time and calculate the adsorption-induced strain and stress.

While Gor and Gurevich (2018) confirmed the validity and applicability of Gassmann theory into channel-like nanoporous media, we found that there exists a breakdown of Gassmann theory in microcracked nanopore-dominated media. To bridge the gap, we verified that P-wave velocity dispersion in such media can be properly modeled in the framework of classical squirt flow theory, which has been validated in many microcracked macropore-dominated media. This enables the possibility of applying the mature theory in conventional rock physics to nanopore-dominated media. We also found it could be possible to extend the applicability of squirt flow theory from contractional to extensional stress regimes, which is crucial to capture the response of microcracked media to fluid substitution from deep underground to near-surface condition.

The transmitted energy changes and corner frequency shift in the direct P waves are well-correlated with moisture-induced strain observed around first Fresnel zone. Both acoustic attributes show amplification, attenuation and recovery in response to the approach of the wetting front. After a comprehensive study of analytical analysis, numerical simulation and experimental observation, we conclude that these two attributes behave in a predictable manner, which is assumed to be associated with the elastic wave propagation near the first Fresnel zone and reflection on the wetting front. This finding provides ability of using elastic waves propagation to quantify elastic changes in porous media as a result of gradual wetting.

Acknowledgments

The authors would like to thank Elsys company, especially Roman Bertschi, for their hardware and software support for this research. The authors are indebted to Mrs. Sally Selvadurai (scientific Editor at Assist-Ed) for her thorough proofreading and editing of the manuscript. Mr. Wu and Dr. Li are financially supported by the chair, Professor Simon Loew, and the China Scholarship Council. This work was supported by Swiss National Science Foundation (SNSF) R 'Equip "Long-term damage evolution in brittle rocks subject to controlled climatic conditions" (Project 170746) and "Physical constraints on natural and induced earthquakes using innovative lab-scale experiments: The LabQuake Machine" (Project 170766).

References

Agersborg, R., Johansen, T. A., Jakobsen, M., Sothcott, J., & Best, A. (2008). Effects of fluids and dual-pore systems on pressure-dependent velocities and attenuations in carbonates. *GEOPHYSICS*, *73*(5), N35-N47. doi: 10.1190/1.2969774

Aki, K., & Chouet, B. (1975). Origin of coda waves: source, attenuation, and scattering effects. *Journal of Geophysical Research: Solid Earth*, *80*(23), 3322–3342.

ASTM D-18. (2008). Standard test method for laboratory determination of pulse velocities and ultrasonic elastic constants of rock. In *Annual book of astm standards* (p. 356–363). ASTM International.

Aydin, A. (2015). Upgraded ISRM Suggested Method for Determining Sound Velocity by Ultrasonic Pulse Transmission Technique. In R. Ulusay (Ed.), *The isrm suggested* *methods for rock characterization, testing and monitoring: 2007-2014* (pp. 95–99). Cham: Springer International Publishing. doi: 10.1007/978-3-319-07713-0{_}6

Barton, N. (2006). *Rock quality, seismic velocity, attenuation and anisotropy.* UK & Netherlands: Taylor & Francis.

Berryman, J. G. (1999). Origin of Gassmann's equations. *GEOPHYSICS*, *64* (5), 1627–1629. doi: 10.1190/1.1444667

Biot, M. A. (1956). Theory of propagation of elastic waves in a fluid saturated porous solid. I. Low frequency range and II. Higher-frequency range. *The Journal of the Acoustical Society of America*, *28* (2), 168–191. doi: 10.1121/1.1908241

Birch, F. (1960). The velocity of compressional waves in rocks to 10 kilobars: 1. *Journal of Geophysical Research (1896-1977)*, *65* (4), 1083–1102. doi: https://doi.org/10.1029/JZ065i004p01083

Blaber, J., & Antoniou, A. (2015). Ncorr instruction manual. *see http://www. ncorr. com/download/ncorrmanual_v1_2_1. pdf*.

Bracewell, R. N. (1986). *The Fourier Transform and its Applications* (Vol. 31999). McGraw-Hill New York.

Burjánek, J., Gischig, V., Moore, J. R., & Fäh, D. (2017). Ambient vibration characterization and monitoring of a rock slope close to collapse. *Geophysical Journal International*, *212* (1), 297–310. doi: 10.1093/gji/ggx424

Burjánek, J., Kleinbrod, U., & Fäh, D. (2019). Modeling the seismic response of unstable rock mass with deep compliant fractures. *Journal of Geophysical Research: Solid Earth*, *124* (12), 13039–13059. doi: https://doi.org/10.1029/2019JB018607

Cadoret, T., Marion, D., & Zinszner, B. (1995). Influence of frequency and fluid distribution on elastic wave velocities in partially saturated limestones. *Journal of Geophysical Research: Solid Earth*, *100* (B6), 9789–9803. doi: https://doi.org/10.1029/95JB00757

Christaras, B., Auger, F., & Mosse, E. (1994). Determination of the moduli of elasticity of rocks. Comparison of the ultrasonic velocity and mechanical resonance frequency methods with direct static methods. *Materials and Structures*, *27* (4), 222–228. doi: 10.1007/BF02473036

Coyner, K. B. (1984). *Effects of stress, pore pressure, and pore fluids on bulk strain, velocity, and permeability in rocks* (Unpublished doctoral dissertation). Massachusetts Institute of Technology.

David, C., Barnes, C., Desrues, M., Pimienta, L., Sarout, J., & Dautriat, J. (2017). Ultrasonic monitoring of spontaneous imbibition experiments: Acoustic signature of fluid migration. *Journal of Geophysical Research: Solid Earth*, *122*(7), 4931–4947. doi: https://doi.org/10.1002/2016JB013804

David, C., Sarout, J., Dautriat, J., Pimienta, L., Michée, M., Desrues, M., & Barnes, C. (2017). Ultrasonic monitoring of spontaneous imbibition experiments: Precursory moisture diffusion effects ahead of water front. *Journal of Geophysical Research: Solid Earth*, *122*(7), 4948–4962. doi: doi:10.1002/2017JB014193

Diederichs, M. S. (2007). Mechanistic interpretation and practical application of damage and spalling prediction criteria for deep tunnelling. *Canadian Geotechnical Journal*, *44*(9), 1082–1116.

Dobrzanski, C. D., Gurevich, B., & Gor, G. Y. (2021). Elastic properties of confined fluids from molecular modeling to ultrasonic experiments on porous solids. *Applied Physics Reviews*, *8*(2), 21317. doi: 10.1063/5.0024114

Gassmann, F. (1951). Elastic waves through a packing of spheres. *GEOPHYSICS*, *16*(4), 673–685. doi: 10.1190/1.1437718

Gor, G. Y., & Bernstein, N. (2016). Revisiting Bangham's law of adsorption-induced deformation: changes of surface energy and surface stress. *Physical Chemistry Chemical Physics*, *18*(14), 9788–9798.

Gor, G. Y., & Gurevich, B. (2018). Gassmann theory applies to nanoporous media. *Geophysical Research Letters*, *45*(1), 146–155. doi: https://doi.org/10.1002/2017GL075321

Gor, G. Y., Huber, P., & Bernstein, N. (2017). Adsorption-induced deformation of nanoporous materials—A review. *Applied Physics Reviews*, *4*(1), 11303. doi: 10.1063/1.4975001

Gor, G. Y., & Neimark, A. V. (2010). Adsorption-induced deformation of mesoporous solids. *Langmuir*, *26*(16), 13021–13027. doi: 10.1021/la1019247

Gurevich, B., Makarynska, D., de Paula, O. B., & Pervukhina, M. (2010). A simple model for squirt-flow dispersion and attenuation in fluid-saturated granular rocks. *GEOPHYSICS*, *75*(6), N109-N120. doi: 10.1190/1.3509782

Han, D.-H. (1987). *Effects of porosity and clay content on acoustic properties of sandstones and unconsolidated sediments* (Unpublished doctoral dissertation). Stanford University.

Hanks, T. C. (1979). b values and ω-γ seismic source models: Implications for tectonic stress variations along active crustal fault zones and the estimation of high-frequency strong ground motion. *Journal of Geophysical Research: Solid Earth*, *84*(B5), 2235–2242.

Häusler, M., Michel, C., Burjánek, J., & Fäh, D. (2019). Fracture network imaging on rock slope instabilities using resonance mode analysis. *Geophysical Research Letters*, *46*(12), 6497–6506. doi: https://doi.org/10.1029/2019GL083201

Häusler, M., Michel, C., Burjánek, J., & Fäh, D. (2021). Monitoring the Preonzo rock slope instability using resonance mode analysis. *Journal of Geophysical Research: Earth Surface*, *126*(4), e2020JF005709. doi: https://doi.org/10.1029/2020JF005709

Johnson, D. L., Koplik, J., & Dashen, R. (1987). Theory of dynamic permeability and tortuosity in fluid-saturated porous media. *Journal of Fluid Mechanics*, *176*(-1), 379. doi: 10.1017/S0022112087000727

Johnston, D. H., Toksöz, M. N., & Timur, A. (1979). Attenuation of seismic waves in dry and saturated rocks: II. Mechanisms. *GEOPHYSICS*, *44*(4), 691–711. doi: 10.1190/1.1440970

King, M. S. (1966). Wave velocities in rocks as a function of changes in overburden pressure and pore fluid saturants. *GEOPHYSICS*, *31*(1), 50–73. doi: 10.1190/1.1439763

Knight, R., & Nolen-Hoeksema, R. (1990). A laboratory study of the dependence of elastic wave velocities on pore scale fluid distribution. *Geophysical Research Letters*, *17*(10), 1529–1532. doi: https://doi.org/10.1029/GL017i010p01529

Kovalyshen, Y. (2018). Comment on "Ultrasonic monitoring of spontaneous imbibition experiments: precursory moisture diffusion effects ahead of water front" by David et al. (2017). *Journal of Geophysical Research: Solid Earth*, *123*(8), 6607–6609. doi: doi:10.1029/2018JB016040

Landrø, M. (2001). Discrimination between pressure and fluid saturation changes from time-lapse seismic data. *GEOPHYSICS*, *66*(3), 836–844. doi: 10.1190/1.1444973

Le Breton, M., Bontemps, N., Guillemot, A., Baillet, L., & Larose, (2021, 5). Landslide monitoring using seismic ambient noise correlation: challenges and applications. *Earth-Science Reviews*, *216*, 103518. doi: 10.1016/J.EARSCIREV.2021.103518

Levitz, P., Ehret, G., Sinha, S. K., & Drake, J. M. (1991). Porous vycor glass: The microstructure as probed by electron microscopy, direct energy transfer, small-angle scattering, and molecular adsorption. *The Journal of Chemical Physics*, *95*(8), 6151–6161. doi: 10.1063/1.461583

Li, Y., Kerry, L., Perras, M. A., & Simon, L. (2022). Effect of ambient humidity on the elasticity of unweathered granite. *Journal of Geophysical Research: Solid Earth*.

Li, Y., Leith, K., Perras, M. A., & Loew, S. (2021). Digital image correlation–based analysis of hygroscopic expansion in Herrnholz granite. *International Journal of Rock Mechanics and Mining Sciences*, *146*, 104859. doi: 10.1016/J.IJRMMS.2021.104859

Loew, S., Gschwind, S., Gischig, V., Keller-Signer, A., & Valenti, G. (2017). Monitoring and early warning of the 2012 Preonzo catastrophic rockslope failure. *Landslides*, *14*(1), 141–154.

Martiartu, N. K., & Böhm, C. (2017). *TTomo: Straight ray tomography.* Seismology and Wave Physics group at ETH Zurich.

Mavko, G., & Jizba, D. (1991). Estimating grain-scale fluid effects on velocity dispersion in rocks. *GEOPHYSICS*, *56*(12), 1940–1949. doi: 10.1190/1.1443005

Mavko, G., Mukerji, T., & Dvorkin, J. (2020). *The Rock Physics Handbook.* Cambridge, United Kingdom: Cambridge University Press. doi: 10.1017/9781108333016

Mavko, G., & Nur, A. (1979). Wave attenuation in partially saturated rocks. *GEOPHYSICS*, *44*(2), 161–178. doi: 10.1190/1.1440958

McBain, J. W., & Ferguson, J. (2002). On the nature of the influence of humidity changes upon the composition of building materials. *The Journal of Physical Chemistry*, *31*(4), 564–590.

Moore, J. R., Geimer, P. R., Finnegan, R., & Michel, C. (2019). Dynamic analysis of a large freestanding rock tower (Castleton Tower, Utah). *Bulletin of the Seismological Society of America*, *109*(5), 2125–2131. doi: 10.1785/0120190118

Moore, J. R., Geimer, P. R., Finnegan, R., & Thorne, M. S. (2018). Use of seismic resonance measurements to determine the elastic modulus of freestanding rock masses. *Rock Mechanics and Rock Engineering*, *51*(12), 3937–3944. doi: 10.1007/s00603-018-1554-6

Müller, T. M., Gurevich, B., & Lebedev, M. (2010). Seismic wave attenuation and dispersion resulting from wave-induced flow in porous rocks - A review. *GEOPHYSICS*, *75*(5). doi: 10.1190/1.3463417

Murphy III, W. F. (1982). *Effects of microstructure and pore fluids on the acoustic properties of granular sedimentary materials* (Unpublished doctoral dissertation). Stanford University.

Nur, A., & Simmons, G. (1969). The effect of saturation on velocity in low porosity rocks. *Earth and Planetary Science Letters*, *7*(2), 183–193. doi: 10.1016/0012-821X(69)90035-1

O'Connell, R. J., & Budiansky, B. (1977). Viscoelastic properties of fluid-saturated cracked solids. *Journal of Geophysical Research*, *82*(36), 5719–5735. doi: https://doi.org/10.1029/JB082i036p05719

Page, J. H., Liu, J., Abeles, B., Herbolzheimer, E., Deckman, H. W., & Weitz, D. A. (1995, 9). Adsorption and desorption of a wetting fluid in Vycor studied by acoustic and optical techniques. *Physical Review E*, *52*(3), 2763–2777. doi: 10.1103/PhysRevE.52.2763

Pimienta, L., David, C., Sarout, J., Perrot, X., Dautriat, J., & Barnes, C. (2019). Evolution in seismic properties during low and intermediate water saturation: competing mechanisms during water imbibition? *Geophysical Research Letters*, *46*(9), 4581–4590. doi: 10.1029/2019GL082419

Pimienta, L., Fortin, J., & Guéguen, Y. (2014). Investigation of elastic weakening in limestone and sandstone samples from moisture adsorption. *Geophysical Journal International*, *199*(1), 335–347. doi: 10.1093/gji/ggu257

Saenger, E. H., Lebedev, M., Uribe, D., Osorno, M., Vialle, S., Duda, M., ... Steeb, H. (2016). Analysis of high-resolution X-ray computed tomography images of Bentheim sandstone under elevated confining pressures. *Geophysical Prospecting*, *64*(4), 848–859. doi: https://doi.org/10.1111/1365-2478.12400

Saito, T. (1981). *Variation of Physical Properties of Igneous Rocks In Weathering.*

Schappert, K., & Pelster, R. (2013). Elastic properties of liquid and solid argon in nanopores. *Journal of Physics: Condensed Matter*, *25*(41), 415302. doi: 10.1088/0953-8984/25/41/415302

Selvadurai, Letendre, A., & Hekimi, B. (2011). Axial flow hydraulic pulse testing of an argillaceous limestone. *Environmental Earth Sciences*, *64*(8), 2047–2058. Retrieved from `https://doi.org/10.1007/s12665-011-1027-7` doi: 10.1007/s12665-011-1027-7

Shabana, A. A. (2018). *Theory of Vibration: An Introduction.* Springer.

Shapiro, S. A. (2003). Elastic piezosensitivity of porous and fractured rocks. *GEOPHYSICS*, *68*(2), 482–486. doi: 10.1190/1.1567215

Spetzler, J., & Snieder, R. (2004). The Fresnel volume and transmitted waves. *GEOPHYSICS*, *69*(3), 653–663. doi: 10.1190/1.1759451

Stoica, P., Moses, R. L., & others. (2005). *Spectral analysis of signals.* Prentice Hall.

Thery, R., Guillemot, A., Abraham, O., & Larose, E. (2020). Tracking fluids in multiple scattering and highly porous materials: Toward applications in non-destructive testing and seismic monitoring. *Ultrasonics*, *102*, 106019. doi: https://doi.org/10.1016/j.ultras.2019.106019

Thommes, M., Kaneko, K., Neimark, A. V., Olivier, J. P., Rodriguez-Reinoso, F., Rouquerol, J., & Sing, K. S. W. (2015). Physisorption of gases, with special reference to the evaluation of surface area and pore size distribution (IUPAC Technical Report). *Pure and Applied Chemistry*, *87*(9-10), 1051–1069. doi: doi:10.1515/pac-2014-1117

Tiennot, M., & Fortin, J. (2020). Moisture-induced elastic weakening and wave propagation in a clay-bearing sandstone. *Géotechnique Letters*, *10*(3), 424–428. doi: 10.1680/jgele.19.00052

Toksöz, M. N., Johnston, D. H., & Timur, A. (1979). Attenuation of seismic waves in dry and saturated rocks: I. Laboratory measurements. *GEOPHYSICS*, *44*(4), 681–690. doi: 10.1190/1.1440969

Walsh, J. B. (1995). Seismic attenuation in partially saturated rock. *Journal of Geophysical Research: Solid Earth*, *100*(B8), 15407–15424. doi: https://doi.org/10.1029/94JB03264

Wang, L., Rybacki, E., Bonnelye, A., Bohnhoff, M., & Dresen, G. (2021). Experimental investigation on static and dynamic bulk moduli of dry and fluid-saturated porous sandstones. *Rock Mechanics and Rock Engineering*, *54*(1), 129–148. doi: 10.1007/s00603-020-02248-3

Winkler, K., & Nur, A. (1979). Pore fluids and seismic attenuation in rocks. *Geophysical Research Letters*, *6*(1), 1–4. doi: doi:10.1029/GL006i001p00001

Winkler, K., & Nur, A. (1982). Seismic attenuation: Effects of pore fluids and frictional-sliding. *GEOPHYSICS*, *47*(1), 1–15. doi: 10.1190/1.1441276

Wu, R., Selvadurai, P. A., Chen, C., & Moradian, O. (2021). Revisiting piezoelectric sensor calibration methods using elastodynamic body waves. *Journal of Nondestructive Evaluation*, *40*(3), 68. doi: 10.1007/s10921-021-00799-1

Wulff, A., & Mjaaland, S. (2002). Seismic monitoring of fluid fronts: An experimental study. *GEOPHYSICS*, *67*(1), 221–229. doi: 10.1190/1.1451622

Yurikov, A., Lebedev, M., Gor, G. Y., & Gurevich, B. (2018). Sorption-induced deformation and eastic weakening of Bentheim sandstone. *Journal of Geophysical Research: Solid Earth*, *123*(10), 8589–8601. doi: doi:10.1029/2018JB016003

Yurikov, A., Lebedev, M., Pervukhina, M., & Gurevich, B. (2019). Water retention effects on elastic properties of Opalinus shale. *Geophysical Prospecting*, *67*(4 - Rock Physics: from microstructure to seismic signatures), 984–996. doi: https://doi.org/10.1111/1365-2478.12673

Zemanek, J., & Rudnick, I. (1961). Attenuation and dispersion of elastic waves in a cylindrical bar. *The Journal of the Acoustical Society of America*, *33*(10), 1283–1288. doi: 10.1121/1.1908417